Dear Dr. Thomas Poulet,

Today, I have uploaded along with the replies to the referees comments and the second revised version of our manuscript gmd-2018-335 title “CobWeb 1.0: Machine Learning Tool Box for Tomographic Imaging”. We think these updates has helped us to further enhance the quality of the manuscript.

In the manuscript, the updated passages are colored in blue and the deleted lines are strikethrough in red.

Best Regards

Swarup Chauhan

We thank the referee for his time, his encouragement w.r.t CobWeb 1.0 and his honest and critical comments. We have done our best to address most of the comments and acknowledge the shortcoming. This has certainly improved the manuscript. Please find below a point-by-point response to your concerns.

Sincerely,

Swarup Chauhan, Kathleen Sell, Wolfram Rühaak, Thorsten Wille and Ingo Sass.

The reviewer comments are formatted in italics and the author's response to the comments are formatted in bold.

Notation RC2.P# represents Reviewers Comment. Paragraph Number

A free, user-friendly toolbox for 3D image processing of X-ray CT imagery of porous rock and sediment is a valuable contribution to the community. The work put into this Cobweb project should definitively be rewarded with a stand-alone paper in GMD that can be cited, whenever the toolbox is used in upcoming projects. This manuscript has already undergone one round of referee comments and revisions. The revised manuscript can still be improved on several occasions, but in general I agree with the present structure of the paper. Also the Cobweb toolbox itself can be improved in many of the routines, which I will list below, but it would be too harsh to reject the paper for that. I would still suggest on more round of revisions to at least discuss these shortcomings more explicitly and also remove grammar/spelling mistakes.

Thanks for the appreciation.

Specific comments:
RC2.P1. I would tone down the novelty aspect of your dual filtering and dual segmentation approach for the gas hydrate data set (e.g. in abstract, P17L3, etc.) To me it rather sounds like a drawback to first filter with an anisotropic diffusion (AD) filter and have unsatisfactory noise removal results so that another non-local means (NLM) filter is required (or vice versa that NLM, which should also be edge-preserving when the parameters are set properly, apparently cannot do a good job without preconditioning with AD). To me dual filtering doesn't sound like something to aspire, but more like extra time required to adjust a larger set of parameters for a satisfactory result. Same holds for dual segmentation. First you have to run unsupervised K-means with many classes, only to regroup them by indexing into meaningful material classes through user interaction by an expert later on.

Revised page 17 line 16 -28

Several attempts were made to remove the edge enhancement effect (ED) using single filters and in combination with supervised techniques. But they did not yield desirable results.

The ED pixels values where in very close vicinity to the Methane Hydrate pixels. Therefore, preprocessing with single filters despite using appropriate settings could not normalize ED to a reasonable range of values (high STDV). So, despite tailoring customized training dataset using a representative slice– due to large stdv of ED values, methane was systematically misclassified as ED as the pixel values deviated away from trained model.

An option was to create different training dataset using several representative slices, and introduce the unknow stack of data for classification in batches of 100 slices. This regularization trick for us did not represent a good norm for supervised ML classification.

Hence, through the experience gained in (Sell et al., 2016) for us dual-filtration was one of the best approaches we could include in preprocessing step. This dual-filtering did not removed the ED completely rather normalize it to a reasonable range. Through the approach of rescaling and (hard) K-means segmentation (dual-segmentation) we were absolutely sure that the ED artifact have been removed.

RC2.P2. I'm not happy with this paragraph on FCM (P6L15-24). First of all, it is hard to follow for a reader that is not already familiar with k-means and fuzzy c-means. Secondly, your basically describing that FCM is incapable of dealing with partial volume voxels at material boundaries being misclassified to the intermediate class (and thus resulting in a too low volume fraction of the darkest class, i.e. porosity), since FCM is only operating in a feature space, i.e. the histogram, and cannot account for spatial features, i.e. partial volume voxels sitting on an edge vs. real intermediate material patches. So all that you can do is to tweak the FCM settings such that the partial volume problems disappear but so do the real intermediate material voxels elsewhere in the image. This drawback seems to be carefully neglected in this paragraph. Maybe remove this paragraph and replaced it with a more general statement, why FCM can be superior to KM.

Revised; Page 6 line 16-20

RC2.P3: It is next to impossible to digest this paragraph on SVM without prior knowledge (P7L19-27).

The explanation given in P7L19-27 is to give the reader an intuitive idea how SVM performs and to restrain the mathematical formulation which is available in the literature; supporting literature has been cited (Suykens and Vandewalle, 1999; van Gestel et al., 2004; Bishop, 2006; Haykin, 1995) (T. M. Cover, 1965) to fulfil the gap in prior knowledge, mathematical formulation and historical significance.

RC2.P3: Take the first sentence, for instance. How can a training dataset be non-linear, what does that actually mean? The training dataset would be a set of gray values that you obtained by clicking into the image and assigning those locations to a certain material class. Those gray values make up a 1D frequency distributions for each material class that can have substantial overlap. Where does the second dimension or even third dimension come from, that help to remove this overlap? See, I'm not even sure if this 2D or 3D coordinate system and the associated hyperplanes are in a feature space or in the spatial domain of the XCT image. Probably, I'm on the wrong track here, but so will be most of the readers.

A dataset can be linearly separable if the points in the dataset can be partitioned into two classes using a threshold function (threshold should not be a piecewise discontinuous function). Loosely speaking the threshold function fits a line to produce the partition.

Now, as pointed out by the reviewer– the training vector is a 1D array of pixels which can have substantial overlap. If I fit a threshold function to this substantially overlapped dataset– this usually leads to wrong partitioning (Bishop, 2006; Haykin, 1995). So, such dataset is regarded as linearly in-separable *alias* non-linear separable dataset (Bishop, 2006). This is what we mean as non-linear training dataset.

Here 3D implies a 2+1 dimensional space which consists of two spatial dimensions that correspond to the coordinated of the pixels position in the image and the third dimension to that of the greyscales that evolves as a result of the machine learning. Since we are having continuous values of the greyscales values we require a sufficiently smooth threshold to make the classification.

RC2.P4: The training is pretty restrictive (P12L1-21). If I understand correctly, you can only click once for one material and the class statistics is constructed from 6x6 pixels around the coordinate, where you clicked. My experience with Ilastik, https://www.ilastik.org/, another free machine-learning based segmentation toolkit, is that you can draw multiple lines of any thickness for each material and all covered pixels/voxels contribute to the class statistics. In addition, a whole set of samples can be segmented at once by only drawing training data in a small number of samples (even in live mode, i.e. the segmentation results are updated on the fly with any additional line. I think it's unfair to criticize this somewhat inflexible training mode in Cobweb. Please take this as an encouragement for further development and add Ilastik to the software survey in the beginning.

We admit, that CobWeb is a bit inflexible and rudimentary in terms of certain features compared to software like Ilastik. In the future versions we can improve these features.

We have added Ilastik to the survey of open source software's. Figure 1b. page 28

RC2.P5: I do not understand the paragraph on 2D slice-by-slice segmentation (P17L14-26)). Do different area fractions of each material (i.e. spatial variability of the rock) or vertical intensity variations (due to hardware shortcomings) mess up the slice-by-slice approach? If it is the former, you need to explain why different area fractions in each slice (e.g. change in porosity) affect the segmentation results, if the average gray value of pores, rocks and matrix does not change. Also, calling the Z coordinate direction in XCT data "temporal information" is very strange.

Revised, Page 18 -Line 8 – 22

We thank the reviewer for his advice, we changed this part of the text to specify the issue more precisely. In short the topic discussed is only related to the fact that processing is done in 2D and the results are later on combined to a 3D result. Since each slice is an snapshot of the total volume fraction of different materials– by performing slice-by-slice segmentation one gets only the partial information (change in porosity) of the total volume fraction of the respective materials. Therefore, averaging helps to obtain the 3D information. Although this approach is favorable in terms of performance it has shortcomings in terms of possible artefacts.

RC2.P6: Chapter 5.3 on Multi-Phase Segmentation: Is this section for all three datasets? If so, what is actually the third material beside pores and rock in Berea sandstone (and Grosmont carbonate rock)? What does it mean that the intermediate class has a Poisson distribution (P18L9)?

It is a bit discouraging to read that the supervised methods did not result in better segmentations then unsupervised K-means (which has been around for many decades and needs to be cleaned up with your supervised dual segmentation strategy in one out of three show case datasets). So my take-home message is that you 'sell' Cobweb as the first ML-only segmentation toolbox for multi-phase segmentation (P1-19-20 in abstract), only to use K-means throughout the paper which is essentially available in all other commercial or non-commercial toolboxes. I think that this is a shot in the foot, *especially since one reason against using the other ML methods in Cobweb is that they are apparently too slow at the moment. Don't you think it would be better to show the LSSVM or ensemble classifier results instead?*

Not revised.

We acknowledge the reviewer's concern. We think within the scope of the paper which introduces CobWeb and edge enhancement segmentation, the detailed verification with LSSVM and ensemble classifiers has been undermined to some extent. But, the previous work Chauhan et al., (2016) based on which the CobWeb is developed; benchmarks different ML algorithms and draws suitable conclusions. Therefore, this gives us the confidence that CobWeb is usable and durable.

RC2.P7. More info on the watershed method is required (P18L31-P19L9). The x-axis in Fig. 6c (pore radius) suggests a maximum inscribed sphere method to me, but the traditional watershed transform on binary data creates irregular shaped fragments. How can an irregularly shaped object have a single pore radius?

Revised Page 19 to page 20 line 1

We have added some more information on the watershed method as suggested by the reviewer. No, the algorithm does not use inscribed sphere method but the traditional watershed transformation as implemented in Rabbani et al., (2014). and assumes the irregular shape as spherical pores.

8. You simply have not reached an REV for PSD histograms within a single slice (P19L12). My educated guess is that PSD requires an even larger REV than porosity, and yet (against your own advice) you show the PSD of each individual slice in an overloaded figure instead of a single PSD for the entire 3D REV. What do you learn from such a figure? This needs to be changed.

Not revised.

Yes, we accepted this as a short coming of the current research work the implementation will be corrected in the future versions. In the discussion (Page 17-18 | 28-5) addressed this issue and averaging helps to obtain the 3D information. Although this approach is favorable in terms of performance it has shortcomings in terms of possible artefacts.

Technical comments:
P2L31: tackle with this -> tackle this

Changed. Page 2 line 31

P3L6: Why is fspecial striked through?

Corrected.

P3L9: This sentence sounds incomplete. Remove 'Despite'?

The sentence has been slightly changed, the changes are marked in blue in the text.

Page 2 line 11 -line 12

P5L4: masking in -> filtering is - Masking is the wrong word here. You convolve the image with a filter kernel (or just apply a filter). Also, I couldn't follow why two Laplace filters are required and how exactly they are implemented. Is it a Laplace-of-Gaussian with two different sigmas, first a large Gaussian sigma for thick edges followed by a lower Gaussian sigma for thin edges? Is the second applied to the result of the first (would make no sense, since all small features are gone) or to the original image and the outcome somehow combined with the outcome of the first?

Revised: Page4 line 28 – page 5 line 2

Obviously, as pointed by the reviewer, irrespective of large sigma or small sigma first, it will lose all the features.

Within the fspeacial routine we use only the averaging filter we have not implemented the Laplacian or sobel filter. Therefore, we do not do any sequential filtering (repeated) on the same image. Within the for-loop each slice gets filtered only once and later are stacked together.

P5L9: Remove 'Whereas,'

Deleted

P5L20: comprises of pixels -> comprises pixels

Changed. Page 5 line 20

P7L15: unknow -> unknown

Changed. Page 7 line 22

P6L30: models -> model's

Changed. Page 7 line 6

P7L19: Remove 'Now,'

Changed. Page 7 line 26

P9L3: atleast -> at least

Changed. Page 9 line 10

P9L22: Mix of present tense and past tense.

modified. Page 10 line 1-2

The accuracy is determined by calculation area under the curve (AUC), and the simplest ~~was to do that is by using~~ way to do this was by using trapezoidal approximation.

P10L21: where -> were

Changed. Page 10 line 28

P11L13: Meaning of densely nested function unclear

Changed. Page 11 line 20

P11L23: The term 'back-end' might be uncommon outside the computer science world.

Page 11 line 32

Changed to at the data access layer (also know as back-end)

P11L25-26: Combine the two sentences into one

Changed. Page 12 line 1-3

It is an easy, one-step process in the case of unsupervised techniques i.e. based on the options selected in the preprocessing *uitable*, the image is filtered and subsequently, segmented.

P11L26: addition -> additional

Changed. Page 12 line 3

P13L10: The beginning of chapter 4 is rather abrupt. I would write a short summary like: "this concludes the description of the Graphical user interface. For more information the user manual can be consulted which is available as supporting information. In the following Cobweb toolbox is demonstrated by means of three showcase examples, which are briefly introduced in terms of underlying research question, imaging settings and challenges for image processing." - or something similar

Thanks for the suggestion. Following sentences have been added. Page 13 line 22 -line 26

This concludes the description of the section toolbox and functionalities. For more information on the usage of the graphical user interface the user manual can be consulted, which is available as supporting information.

In the following, sections the CobWeb toolbox is demonstrated by means of three showcase examples, which are briefly introduced in terms of underlying imaging settings, research question and challenges for image processing.

P13L22: Write out ED at first occurrence of the abbreviation

For consistency the abbreviation ED has been remove from the manuscript

P15L8: Remove 'Now,'

Removed. Page 15 line 22

P15L28 10243 ->1024^3

Done. Page 16 line 10

P18L9: Do you mean really mean 'low sample size' or 'low volume fraction'?

This is not necessarily the case. A counter example would by a mud-rock with a large volume fraction of the matrix (intermediate class) with low porosity and a few inherent dense rocks.

Changed, page 19 line 4

Yes. low volume fraction is the appropriate word. The wording has been replaced in the manuscript.

P19L4: Explanation is required, why it is so much lower than the porosity values given previously in the material description (mostly due to sub-resolution pores, I guess).

Thanks for the pointers. Following explanation has been added to page 20 line 3 - 6

Particularly, in the case of Grosmount, after segmentation the obtained porosity value φ =10.5 ± 2.3 % is extremely low compared to the laboratory measurement φ =21 % published in (Andrä et al., 2013). Exact reason is not known but could also be partly attributed to sub-resolution pores which couldn't be captured do to low resolution obtained through XCT measurement.

P19L29: These discrepancies in modelling and transport simulation have not been addressed in the main paper. Thereof it is not appropriate to mention them all of a sudden in the conclusions.

It has been removed. Page 20 | L30

Fig3: What do the different blue colors for different boxes stand for?

The figure has been rectified and caption has been updated. Page 30

Fig5: The color bar is misleading. There are only three materials and not five. You might need to create your own color legend if the built-in matlab functionality is not flexible enough to do that. I'm not sure what rescaled (Fig. b) means in this context. Should be explained in the caption.

The color bar has not been changed. The caption has been modified as follows. Page 32

Figure 1: 2D slices of REV 1 are represented above. The raw image is first filtered with anisotropic diffusion filtered and later on with non-local means. Thereafter, the different phases where segregated using a segmentation and indexing approach and the raw image(s) is rescaled such that they aren't any overlap or mixed phases within the raw image; and example is shown as the rescaled 2D ROI plot. Thereafter K-means segmentation is performed on the complete stack; 2D images of slice 1, slice 20 and slice 695 are shown as examples.

References

Andrä, H., Combaret, N., Dvorkin, J., Glatt, E., Han, J., Kabel, M., Keehm, Y., Krzikalla, F., Lee, M., Madonna, C., Marsh, M., Mukerji, T., Saenger, E. H., Sain, R., Saxena, N., Ricker, S., Wiegmann, A., and Zhan, X.: Digital rock physics benchmarks—Part I: Imaging and segmentation, Benchmark problems, datasets and methodologies for the computational geosciences, 50, 25–32, doi:10.1016/j.cageo.2012.09.005, 2013.

Bishop, C. M.: Pattern Recognition and Machine Learning (Information Science and Statistics), Springer-Verlag, Berlin, Heidelberg, 2006.

Chauhan, S., Rühaak, W., Anbergen, H., Kabdenov, A., Freise, M., Wille, T., and Sass, I.: Phase segmentation of X-ray computer tomography rock images using machine learning techniques: an accuracy and performance study, Solid Earth, 7, 1125–1139, doi:10.5194/se-7-1125-2016, 2016.

Haykin, S. S.: Neural networks: A comprehensive foundation, [Nachdr.], Macmillan, New York, NY, 696 pp., 1995.

Rabbani, A., Jamshidi, S., and Salehi, S.: An automated simple algorithm for realistic pore network extraction from micro-tomography images, Neural network applications to reservoirs: Physics-based models and data models, 123, 164–171, doi:10.1016/j.petrol.2014.08.020, 2014.

Sell, K., Saenger, E. H., Falenty, A., Chaouachi, M., Haberthür, D., Enzmann, F., Kuhs, W. F., and Kersten, M.: On the path to the digital rock physics of gas hydrate-bearing sediments – processing of in situ synchrotron-tomography data, Solid Earth, 7, 1243–1258, doi:10.5194/se-7-1243-2016, 2016.

Suykens, J. A. K. and Vandewalle, J.: Least Squares Support Vector Machine Classifiers, Neural Processing Letters, 9, 293–300, doi:10.1023/A:1018628609742, 1999.

T. M. Cover: Geometrical and Statistical Properties of Systems of Linear Inequalities with Applications in Pattern Recognition, IEEE Transactions on Electronic Computers, EC-14, 326–334, doi:10.1109/PGEC.1965.264137, 1965.

van Gestel, T., Suykens, J. A. K., Baesens, B., Viaene, S., Vanthienen, J., Dedene, G., Moor, B. de, and Vandewalle, J.: Benchmarking Least Squares Support Vector Machine Classifiers, Mach. Learn., 54, 5–32, doi:10.1023/B:MACH.0000008082.80494.e0, 2004.

Dear Dr Kirill Gerke,

Thanks. We have added the references and updated the Figure 1.

Sincerely,

Swarup Chauhan, Kathleen Sell, Wolfram Rühaak, Thorsten Wille and Ingo Sass.

Notation *RC1.P#* represents Reviewers Comment. Paragraph Number

I think Authors did quite a job to address the comments of all three reviewers.
It did improve the paper. While i personally would argue with a couple of statements, i think it deserves to be published and total agreement between authors and reviewers should not be a requirement.
If the software in the paper would be written in some interpretable language and not in proprietary Matlab - it would be even better then it is now.

Just one small thing:
RC1.p1: I saw Authors adding FDMSS to Fig.5 and thank then for this help in reaching potential users. But i have to admit that FDMSS solves only single-phase flow problem and do not possess any image processing functionality expect for creation of 3d input image out of 2d images stack. For this it looks rather unfair to see FDMSS's "level" to be higher than the of OpenPNM, which does have a wider range of functionality...

The reviewer meant Fig. 1 instead of Fig. 5; Fig. 1 has been modified.

I also did not see FDMSS and OpenPNM's references in the reference and would for OpenPNM would suggest to cite Jeff's Gostick, J. T. (2017). Versatile and efficient pore network extraction method using marker-based watershed segmentation. Physical Review E, 96(2), 023307 as it adds the major functionality to the package.

Revised. Page 20 line 28-29

All in all, from my point of view the paper is good to go.

CobWeb 1.0: Machine Learning Tool Box for Tomographic Imaging

Swarup Chauhan[1,2], Kathleen Sell[1,3,*], Wolfram Rühaak[4], Thorsten Wille[5], Ingo Sass[2]

[1] Institute for Geosciences, Johannes Gutenberg-University, Mainz 55099, Germany
[2] Institute of Applied Geosciences, University of Technology, Darmstadt 64287, Germany
[3] igem – Institute for Geothermal Resource Management, Berlinstr. 107a, Bingen 55411, Germany
[4] Bundesgesellschaft für Endlagerung mbH (BGE), Peine 38226, Germany
[5]APS Antriebs-, Prüf- und Steuertechnik GmbH, Götzenbreite 12, Göttingen-Rosdorf 37124, Germany

* now at: Ministry of Economic Affairs Rhineland Palatine, Stiftsstrasse 9, Mainz 55116, Germany
~~** now at: Bundesgesellschaft für Endlagerung mbH (BGE), Peine 38226, Germany~~

*Correspondence to: Swarup Chauhan (ssschauhan@gmail.com)

Abstract.

Despite the availability of both commercial and open source software, an ideal tool for digital rock physics analysis for accurate automatic image analysis at ambient computational performance is difficult to pin point. More often image segmentation is driven manually where the performance remains limited to two phases. Discrepancies due to artefacts causes inaccuracies in image analysis. To overcome these problems, we have developed CobWeb 1.0 which is automated and explicitly tailored for accurate grayscale (multi-phase) image segmentation using unsupervised and unsupervised machine learning techniques. The simple and intuitive layout of the graphical user interface enables easy access to perform Image enhancement, Image segmentation and further to obtain the accuracy of different segmented classes. The graphical user interface enables not only processing of a full 3D digital rock dataset but also provides a quick and easy region-of-interest selection, where a representative elementary volume can be extracted and processed. The CobWeb software package covers image processing and machine learning libraries of MATLAB® used for image enhancement and image segmentation operations, which are compiled into series of windows executable binaries. Segmentation can be performed using unsupervised, supervised and ensemble classification tools. Additionally, based on the segmented phases, geometrical parameters such as pore size distribution, relative porosity trends and volume fraction can be calculated and visualized. The CobWeb software allows the export of data to various formats such as ParaView (.vtk), DSI Studio (.fib) for visualization and animation and Microsoft® Excel and MATLAB® ® for numerical calculation and simulations. The capability of this new software is verified using high-resolution synchrotron tomography datasets, as well as lab-based (cone-beam) X-ray micro-tomography datasets. Albeit the high spatial resolution (sub-micrometer), the synchrotron dataset contained edge enhancement artefacts which were eliminated using a novel dual filtering and dual segmentation procedure.

1. Introduction

Currently a vast number of available commercial and open source software packages for pore-scale analysis and modelling exists (compiled in Figure 1), but dedicated approaches to verify the accuracy of the segmented phases are lacking. To the best of our knowledge, the current practice among researchers is to alternate between different available software tools and to synthesize the different datasets using individually aligned workflows. Porosity and in particular, permeability can vary dramatically with small changes in segmentation, as significant features on the pore-scale get lost when thresholding greyscale tomography images to binary images, even if using the most advanced data acquiring techniques like synchrotron tomography (Leu et al., 2014). Our new CobWeb 1.0 visualization and image analysis toolkit addresses some of the challenges of selecting representative elementary volume (REV) for X-ray computed tomography (XCT) datasets reported earlier by several researchers (Zhang D et al., 2000; Gitman et al., 2006; Razavi et al., 2007; Al-Raoush and Papadopoulos, 2010; Costanza-Robinson et al., 2011; Leu et al., 2014). The software is built on scientific studies which have been peer-reviewed and accepted in the scientific community (Chauhan et al., 2016b; Chauhan et al., 2016a). The spinoff for these studies was not the lack of accuracy provided by manual segmentation schemes, but the subjective assessment and non-comparability caused by the individual human assessor. Therefore, an automated segmentation schemes offer speed, accuracy and possibility to intercompare results, enhancing traceability and reproducibility in the evaluation process. To our knowledge none of the XCT software used in rock science community relies explicitly on machine learning to perform segmentation, which makes the software unique.

Despite many review articles and scientific publication highlight potential of machine learning and deep learning (Iassonov et al., 2009; Cnudde and Boone, 2013; Schlüter et al., 2014), software libraries or toolbox are seldom made available. Thus, with CobWeb we started for the first time to fill this gap, and despite its limited volume rendering capabilities— it is a useful tool and current version of the software can be applied in scientific and industrial studies. CobWeb provides an appropriate test platform, where new segmentation and filtration schemes can be tested and used as a complementary tool to the simulation software GeoDict and Volume Graphics. The simulation softwares (GeoDict and Volume Graphics) have benchmarked solvers for performing flow, diffusion, dispersion, advection type simulation, but their accuracy relies heavily on the finely segmented datasets. This software is based on a machine learning approach with great potential for segmentation analysis as introduced previously (Chauhan et al., 2016b; Chauhan et al., 2016a). Further, this software tool package was developed on a MATLAB® workbench and can be used as Windows stand-alone executable (.exe) files or as a MATLAB® plugin. The dataset for the gas hydrate sediment (GH) geomaterials was acquired using monochromatic synchrotron X-ray, unhampered by beam hardening; (Sell et al., 2016) highlighted problems with edge enhancement ~~(ED)~~ artefact and recommended image morphological strategies to tackle this challenge. In this paper, we describe therefore also a strategy to eliminate ED artefacts using the same dataset but applying the new machine learning approach.

2. Image Processing

Image pre-processing is one of the essential and precautionary steps before image segmentation (Iassonov et al., 2009; Schlüter et al., 2014). Image enhancement filtering techniques help to reduce artefacts such as blur, background intensity and contrast variation. Whereas, denoise filter such as median filter, non-local means filter, and anisotropic diffusion filter can assist in lowering the phase misclassification and improving the convergence rate of automatic segmentation schemes. CobWeb 1.0 is equipped with image enhancement and denoise filters, namely*, imsharpen, non-local-means, anisotropic diffusion and fspecial*, which are commonly used in the XCT image analysis community.

2.1.1. Imsharpen Image Enhancement

Despite at the instrument level different measures can be taken to improve resolution of the X-ray volumetric data, the contrast, in the XCT images depends particularly on the composition and corresponding densities (optical depth) of the test sample. Therefore, it is somewhat difficult to enhance contrast at the experimental setup or at the x-rays system design control stage. Thus, the contrast needs to be enhanced or adjusted after the volumetric image has been generated. For this purpose, image sharpening can be used. Image sharpening is a sort of contrast enhancements. The contrast enhancements generally takes places at the contours, were high and low greyscale pixel values intensities meet (Parker, 2010).

2.1.2. Anisotropic Diffusion Image Filtering

For intuition purposes, Anisotropic Diffusion filter (AD) can be thought as (Gaussian) blur filter. AD blurs the image, where it carefully smooths the textures in the image by preserving its edges (Kaestner et al., 2008; Porter Mark L. et al., 2010; Schlüter et al., 2014). To achieve the smoothing along edge preservation, the AD filter performs an iteration to solve non-linear partial differential equations (PDE) of diffusion:

$$\frac{\partial I}{\partial t} = c(x, y, t)\Delta I + \nabla c \,.\, \nabla I \tag{1}$$

Where,

I is the image, t is the time of evolution and c is the flux which controls the rate of diffusion at any point in the image.

(P. Perona and J. Malik, 1990) introduce a flux function c to follow an image gradient and stop or restrain the diffusion when it reaches the region boundaries (edges preservation).

Given by

$$c(\|\nabla I\|) = \ e^{-(\|\nabla I\| \ \kappa)^2} \tag{2}$$

$$(\|\nabla I\|) = \frac{1}{1+(\frac{\|\nabla I\|}{\kappa})^2} \tag{3}$$

Here, the parameter κ is a tuning parameter that determines if the given edge to be considered as a boundary or not. Large value of κ lead to an isotropic solution and the edges are removed. For our investigations the parameter κ (threshold stop) was fixed to the value 22 968, which is the edge preservation limit between quartz grain and hydrate phase. The desired denoising (bluring/smoothing) was achieved within five iteration steps.

2.1.3. Nonlocal Means Image Filtering

Nonlocal means (NLM) filter is based on the assumption that the image contain an extensive amount of self-similarity (A. Buades et al., 2005; Shreyamsha Kumar, 2013). Based on this assumption (A. Buades et al., 2005) extended the linear neighborhood SUSAN filter (Smith and Brady, 1997) with nonlocal class. Thus, through the nonlocal class, the spatial search for similar pixel values is not restricted to a constrained neighborhood pixel but the whole image is part of the search for similar pixel values. Given by the equation

$$NL(i) = \sum_{j \in I} w(i,j)v(j) \qquad (4)$$

Where,

$NL(i)$ is the estimated nonlocal intensity of the pixel *i*

I is the image

$w(i,j)$ is the weight (or average value) applied to noisy image $v(j)$ to obtain and restore the pixel *i*.

However, for practical and computational reason, the search is performed within a search window or neighborhood patches, and $w(i,j)$ evaluates similarity in pixel intensities between of local neighborhood patches. Where the weight $w(i,j)$ is calculated as

$$w(i,j) = \frac{1}{Z(i)}\, e^{-\frac{\left\|v(N_i)-v(N_j)\right\|_{2,\sigma}^2}{h^2}} \qquad (5)$$

Where. $Z(i)$ is a normalization constant

$$Z(i) = \sum_j e^{-\frac{\left\|v(N_i)-v(N_j)\right\|_{2,\sigma}^2}{h^2}} \qquad (6)$$

$v(N_i)$, $v(N_j)$ are the local neighborhood patches.

The similarity is fulfilled as the Euclidean distance between the local neighborhoods patches exponentially decreases.

$\sigma > 0$ is the standard deviation.

In eq. (5) and (6), the distance function $\left\|v(N_i) - v(N_j)\right\|^2$ is pointwise multiplied (convolved) with σ, to ensure fair contribution of pixel values to the weighted function.

2.1.4. fspecial Image Filtering

fspecial helps in creating 2D high pass and low pass filters. High pass filters are used for sharpening and edge detection, whereas low pass filters are used for smoothing the image quality. Frequently used high pass filters are Laplacian and Sobel masks (kernel), and most often used low pass filter is the Gaussian smoothing mask (mask). However, in n the current version of CobWeb, fspecial is implemented as an averaging filter. The filter is directly applied on the 2D slices without any convolution with the filter kernel.

~~Laplacian mask can be mathematically formulated as~~

~~$L(x,y) = \frac{\partial^2 I}{\partial x^2} + \frac{\partial^2 I}{\partial y^2}$ (7)~~

~~Where $L(x,y)$ is the Laplacian of pixels with intensity $I(x,y)$~~

~~The first and second derivative implies that the masking in done twice, adding the first mask to the original image enhance thick edges in the image, and further adding the mask second time to the modified images sharpens fine details of the image. Thereby, sharpening edge contours of different intensities which were previously blurred in the original image. The Sobel filter eases edge detection in horizontal and vertical direction in regions of high pixel gradient (edges).~~

~~Whereas, Gaussian 2D smoothing operator is used to smooth images in order to remove details and noise. This done by adding a mask (kernel) to the original image. This transformation stretches the pixel values of the original image to an extent that they appear smoothened. The mask is a 2D Guassian (circular symmetric) operator mathematically formulated as~~

~~$g(x,y) = \frac{1}{\sqrt{2\pi\sigma}} e^{\frac{-d^2}{2\sigma^2}}$ (8)~~

~~$d = \sqrt{(x - x_c)^2 + (y - y_c)^2}$ (9)~~

~~Where (x,y) are the pixels, σ is the standard deviation in the intensity of the pixels, d is the distance calculated between then neighborhood pixels to the center of the pixel $(x_c\ ,\ y_c)$. So, the higher the σ standard deviation of the pixel intensities the smoother is the transformed image.~~

2.2. Image Segmentation

Digital image comprises ~~of~~ pixels of color or greyscale intensities. Image segmentation is partitioning or classification the pixel intensities into disjoint regions that are homogenous with respect to some characteristics (Bishop, 2006). There is continuous research efforts done in various international groups to improve and developed image segmentation approaches (Mjolsness and DeCoste, 2001). In particular, the most popular and relevant image segmentation approaches for analyzing X-ray tomographic rock images is presented in the review studies done by (Iassonov et al., 2009) and (Schlüter et al., 2014). We use machine learning techniques for image segmentation and have implemented algorithms such as K-means, Fuzzy C-means (unsupervised), least square support vector machine (LSSVM) (supervised), bragging and boosting (esamble classifiers) for automatic segmentation Chauhan et al., (2016a), (Chauhan et al., 2016b) and references within. The performance of these machine learning technique can be assesed by matrices such as, entropy, receiver operational charesteristics (ROC), 10-fold crossvalidation (Chauhan et al., 2016b). Below all the above mentioned algorthms are discribed in brief.

2.2.1. Unsupervised Machine Learning Techniques

K-means is one of the simplest, yet, robust unsupervised machine learning (ML) algorithms commonly used in partitioning data (MacQueen, 1967; Jain, 2010; Chauhan et al., 2016b). Through an iterative approach the K-means algorithm computes the Euclidean distance between the data points (pixel value) to its nearest centroid (cluster). The iteration converges when the objective function, i.e. the mean square root error of Euclidean distance, reaches the minimum. This is, when each of the pixel in the dataset is assigned to its nearest centroid (cluster). However, the K-means algorithm has the tendency to converge at local minima without reaching the global minimum of the objective function. Therefore, it is recommended to repeatedly run the algorithm to increase the likelihood that the global minimum of the objective function will be identified. The performance of the K-means algorithm is influenced predominantly by the choice of the cluster centers (Chauhan et al., 2016b).

The Fuzzy C-means (FCM) clustering procedure involves minimizing the objective function (Dunn, 1973)

$$J_{fcm}\,(Z;U;V) = \sum_{j=1}^{n}\sum_{i=1}^{k}(\mu_{ij})^{m}\ \left\|x_i{}^{(i)} - c_k\right\|^2 \qquad (10)$$

where $c_k = \sum_{j=1}^{n} u_{ij} x_i$

c_k is the k^{th} fuzzy cluster centre, m is the fuzziness parameter, $m.u_{ij}$ is the membership function.

Unlike k-means, FCM performs a sort of soft clustering, in the FCM iterative scheme each data point can be a member of multiple clusters (Dunn, 1973; Bezdek et al., 1987; Jain et al., 1999; Jain, 2010). This notion of Fuzzy clustering can be controlled by using a membership function (Zadeh, 1965). The membership value ranges between [0,1] and by selecting different membership values, the distance function can be regularized “loosely” or “tightly” and certain material phases with low volume fraction can be conserved from being clustered in adjoin cluster boundaries. However, it is essential to test different combination of membership values with several centroid centres (segmentation classes) to obtain reliable results. ~~So, for example, a tight sandstone rock sample with a mean diameter and height of 4-5 cm respectively, with high density and relative porosity less then 6% will result in XCT tomograms of voxel resolution of ~13 µm with very low contrast. The low contrast, makes it difficult to identify pixel gradients. Since an intermediate phase pixel in between the gradient exists. These intermediate phases pixels in physical sense can represent connectivity in between the pores. If Kmeans is used, it performs a conservative segmentation and closes such connectivity by classifying them with absolute low intensity pixels (pores). Therefore, it can be beneficial to used FCM algorithm. FCM has a membership function and by selecting different membership values, the distance function can be regularized “loosely” or “tightly” and the intermediate pixel (connectivity) can be preserved. However, it is essential to test different combination of membership values with several centroid centres (segmentation classes) to obtain reliable results.~~

2.2.2. Supervised Machine Learning Technique

Similar to unsupervised techniques, the objective of supervised machine learning technique is to separate data. The advantage supervised technique offers compared to unsupervised technique is that, it is effective in separating non-linear separable data (Haykin, 1995; Bishop, 2006). In supervised technique the prediction is made by a model. The model is a mathematical function, which fit a line or a plane in between linearly or non-linearly separable data to classify them into different categories. The model's ability or intuition, where to place the line or plane in between the dataset to clearly separate (classify) them− is based on its (model) apriori knowledge of the dataset− this apriori knowledge is called the training dataset. Therefore, unlike unsupervised technique, the supervised model needs be trained on a subset of the dataset. The training dataset, is the only 'window' through which, the model knows some pattern about the linear or non-linear separable dataset. How good, the model has acquired the knowledge of the training dataset, determines its success in prediction. If it has learned the training data accurately, it picks up noise along with the pattern and loose it ability of generalization, thus fails when introduce to (unknow) separable-dataset. Alternatively, if the model has 'vaguely' learnt the training dataset; could be due very less training dataset, or if the model is to simple or complex to learn. This could also lead to the failure in prediction. Therefore, to manage a good tradeoff, cross-validation techniques are used to monitor the learning rates of the model (Haykin, 1995).

Support vector machine (SVM) (Haykin, 1995) and its modified version least square support vector machine (LSSVM) are one such category of supervised ML technique (Suykens and Vandewalle, 1999) and use the principles mentioned above. The plane separating the data is termed as hyperplane. The hyperplane has a boundary around it, which is called the *margin* and the data points that lie closest or on the margin are called the *support vectors*. The width of the margin governs the tradeoff, i.e. if the model is overfitted or underfitted to the training dataset; and can be verified through cross-validation techniques. If the width of the margin is two narrow (high learning rate), the model is overfitted (high variance) to the training dataset and will loose it generalization capability and may not separate the linear or non-linear separable (unknown) data accurately. If the width of the margin is too wide (very low learning rate), the model is underfitted (high bias) to the training dataset and will fail. Optimal learn model has a just the appropriate width, to maintain the generalization and also learn the patterns in the dataset.

~~Now,~~ If the training dataset is non-linear and inseparable in 2D coordinate system, it is useful to project the dataset in 3D coordinate system− thus, by doing so, the added dimension (3D) helps to visualize the data and find a place fit an hyperplane to separate them (T. M. Cover, 1965). So, SVM and LSSVM use the principle of cover theorem (T. M. Cover, 1965) to project the data in to higher dimension to make them linearly separable and transform them back the original coordinate system (Suykens and Vandewalle, 1999). Hence what type of projection is to be performed by the SVM or LSSVM is done by choosing appropriate kernel function (van Gestel et al., 2004). This gives them the capability to attain the knowledge of the data and also preserve the generalization behaviour of the model or the classifier. In the original or the 2D coordinate system, the hyperplane, is no longer a line but a convex shaped curved which has clearly, separated the data and suitable margins to the support vectors.

2.2.3. Ensemble Classifiers Technique

As the name implies ensemble classifiers is an approach, where the decision of several simple models is considered to improve the prediction performance. The idea behind using ensemble methods emulates from a typical human approach of exploring several options before making a decision. The ensemble technique is faster compared to supervised techniques. Basically, the evaluation of the decisions predicted by the simple models can be either done sequentially (Bragging or Boosting) or in parallel (Random Forest). Our toolbox used the sequential approach with a variation Bragging and Boosting for classification. These Bragging and Boosting used tree learners (Seiffert et al., 2008; Breiman, 1996), inherited from the MATLAB® libraries. The main difference between Bragging and Boosting are as follows. Bragging generates a set of simple models, first trains these models with the random sample and evaluates the classification performance of each model using the test subset of data. In the second step only those models whose classification performance was low are retrained. The final predictive performance rate of the Bragging classifier− is an average of individual model performances. This approach minimizes the variance in the prediction−, meaning if several Bragging classifiers are generated from same sample of data−, their prediction capability when exposed to unknow dataset will not differ much. The main different of Boosting to Bragging is that; Bragging retrain selected models (high misclassification rate) with the complete training dataset until their respective accuracy increases. Whereas, in Boosting the size of the data which has been misclassified in increased in ratio to the data which has been accurately classified− and thereafter *all* the models are retrained sequentially. The predictive performance is calculated same as in Bragging by averaging the predictive performance rate of the individual models. This approach of Boosting minimizes the bias in the prediction.

2.3. Performance

It is necessary to monitor the performance of an ML model. This ensures that the trained modelled does not overfit or underfit with the training dataset. The main reason for overfitting and underfitting of the model with the training dataset is directly proportional to the complexity of the ML models. However, the consequence is that an overfitted trained ML model will capture noise along with the information pattern from the training dataset and will lose it ability of generalizability. Hence leading to inaccurate classification when exposed to unknow dataset; as it has high variance toward the training dataset. On the opposite side, when the ML model underfit with the training dataset, it is unable to learn or capture the essence of the training dataset; this can happen either due to a choice of a simple type model (E,g linear instead of quadratic) or very less amount of data to build a reliable model. As a consequence the ML fails to predict as it has low variance towards the training dataset (Dietterich, 1998). So, the performance of the ML model; (low variance and low bias) is an indication how accurate it can predict. The above explanation is valid for supervised ML techniques. For unsupervised clustering techniques where there isn’t any model available to train. The quality of the classification is judge from the classified result. One such commonly used metrics is the Entropy (Stehl 2002; Meila 2003 and Amigó et al., 2009). In CobWeb, the performance of the ML models and the quality of the classification can be evaluated using 10-fold Cross Validation, Entropy, Receiver Operational Characteristics (ROC). The explanation of these methods are briefly described in the subsection below. For detailed information the readers are referred to Stehl (2002) (Dietterich, 1998; Bradley, 1997) and references within.

2.3.1. 10-K fold Cross-Validation

The idea for K-fold cross-validation was first recommended by Larson (1931). K-fold cross validation is a performance evaluation technique which check the overfitting and underfitting of the ML model. In the K-fold technique, the training data is divided into k partitions. Thereafter, the ML model is trained with k-1 partition of data, and tested on a withheld kth subset of data that has not been use for training. This process is repeated k-times, through this each datapoint in the training dataset get to be tested at least once, and is used, for training k-1 times. As it can be seen, this approach should significantly reduce the overfitting (low variance) as most of the data is used for testing and underfitting (low bias) as almost all the data is used for training. As from empirical evidence in k = 10 is preferred.

2.3.2. Entropy

The Entropy of a class reflects how the members of the k pixels are distributed within each class; the global quality measure is by averaging the entropy of all classes.

$$\text{Entropy} = -\sum_j \frac{n_j}{n} \sum_i P(i,j) \times \log_2 P(i,j) \qquad (11)$$

Where $P(i,j)$ is the probability of find an item from the category i in the class j, where n_j is the number of items in class j and n the total number of items in the distribution.

2.3.3. Receiver Operational Characteristics

Receiver Operational Characteristics (ROC) curves is one of the popular methods to cross-validation of ML model performance (probability of models correct response $P(C)$ to the predicted result) (Bradley, 1997). It has three variables:

$$\text{Accuracy (1 - Error)} = \frac{T_p+T_n}{C_p+C_n} = P(C) \qquad (12)$$

$$\text{Sensitivity } (1 - \beta) = \frac{T_p}{C_p} = P(T_p) \qquad (13)$$

$$\text{Specificity } (1 - \alpha) = \frac{T_n}{C_n} = P(n) \qquad (14)$$

Where, $T_p\ and\ T_n$ are the true positive and true negative examples and $C_p\ and\ C_n$ are total number of true positive and true negative examples obtained from the training dataset.

Probability of false positive is $P(F_p) = \alpha$

Probability of true positive is $P(T_p) = (1 - \beta)$

The accuracy is determined by calculation area under the curve (AUC), and the simplest ~~was to do that is by using~~ way to do this was by using trapezoidal approximation.

$$\mathrm{AUC} = \sum_i \left\{(1 - \beta_i \cdot \Delta\alpha) + \frac{1}{2}(\Delta(1 - \beta).\ \Delta\alpha)\right\} \qquad (15)$$

3. Toolbox and functionalities − CobWeb Key Features

The first version of CobWeb offers the possibility to read and to process reconstructed XCT files in both .tiff and .raw formats. The graphical user interface (GUI) is embedded with visual inspection tools to zoom in/out, cropping, color, and scale, to assist in the visualization and interpretation of 2D and 3D stack data. Noise filters such as non-local means, anisotropic diffusion, median and contrast adjustments are implemented to increase the signal-to-noise ratio. The user has a choice of five different segmentation algorithms, namely K-means, Fuzzy C-means (unsupervised), least square support vector machine (LSSVM) (supervised), bragging and boosting (ensemble classifiers) for accurate automatic segmentation and cross-validation. Relevant material properties like relative porosities, pore size distribution trends, volume fraction (3D pore, matrix, mineral phases) can be quantified and visualized as graphical output. The data can be exported to different file formats such as Microsoft® Excel (.xlsx), MATLAB® (.mat), ParaView (.vkt) and DSI studio (.fib). The current version is supported for Micosoft® Windows PC operating systems (Windows 7 and 10).

The main GUI window panel divides into three main parts (Figure 2), the tool menu strip, the inspector panel, and the visualization panel. The tool strip contains menus for zoom in and out, pan, rotate, point selection, color bar, legend bar, and measurement scale functionalities. The inspector panel is divided into subpanels where the user can configure the initial process settings such as segmentation schemes (supervised, unsupervised, ensemble classifiers), filters (contrast, *non-local means*, *anisotropic* filter, *fspecial*), and distance functions (link distance, Manhattan distance, box distance) to assist segmentation and geometrical parameter selection for image analysis (REV, porosity, pore size distribution (PSD), volume fraction). The display subpanel *records*, displays the 2D video of the XCT stack and the respective histogram. History subpanel is a *uilistbox* that displays errors, processing time/status, processing instruction, files generated/exported and executed callbacks. Control subpanel is an assemblage of *uibuttons* to initialize the XCT data analysis process and the progress bar. Visualisation panel is where the results are displayed in several resized windows, which can be moved, saved or deleted. The pan-windows displayed inside the visualization module are embedded with *uimenu* and *submenu* to export, plot and calculate different variables like porosity, PSD, volume fraction, entropy, or receiver operational characteristics. To get the desired user functionalities, MATLAB® internal user-interface libraries were inadequate. Therefore, numerous specific adaptions are adopted from Yair Altman's undocumented MATLAB® website and the MATLAB® File Exchange community. Specifically, the GUI Layout Toolbox of David Sampson is used to configure the CobWeb GUI layout; the preprocessing *uitable*, uses the MATLAB® java-component; it was designed using *uitable* customization report provided by (Altman, 2014).

As a stand-alone, the CobWeb GUI can be executed on different PC and HPC clusters without any license issues. The framework of CobWeb 1.0 is schematically illustrated in Figure 3 and the direction for the arrow (left to right) represents the series in which the various functions are executed. The backend architecture can be broadly classified in to three different categories, namely:

- Control module
- Analysis module
- Visualization module

3.1.1. Control module

Initially, the main figure panel is generated, followed by the tool strip dividing the main figure into different panels and subpanels as shown in Figure 2. After that, the control buttons *Load*, *Start*, *Stop*, *Volume Rendering* and *Clear* are created, initialized and the relevant information is appended in a main structure. Ideally, at this point, any button can be triggered or activated. However, on doing so, an exception will be displayed in the history subpanel, indicating the next arbitrary steps. That is, to first load the data by pressing the *Load* button, where the *Load* function checks the file properties, loads the data in .tiff and .raw format, creates and displays 2D video of the selected stack, save the video file in the current folder, and updates the respective variables to the main structure. The *Stop* button (*Stop* function) ends the execution. However, when the processing is inside a loop, the *Stop* function can break the loop only after the i-th iteration. The *Clear* button (*Clear* function), deletes the data and clears all the variables in the main structure, resetting the graphical window.

3.1.2. Analysis module

The next step is data processing; triggered by pressing the *Start* button, which activates the *Start* function. The *Start* function concatenates the entire analysis procedure and is shown as Start () in Figure 3. is a function of densely nested loops, ~~where~~ the bullet points and the sub-bullet points shown in Figure 3, symbolizes the outer and the inner nested loops. Initially, the data is gathered and a sanity check is performed to evaluate, if the user, selected the relevant checkboxes and respective suboptions in the preprocessing *uitable*. If, the checkboxes are not selected, an exception alert is displayed in the *History* panel, highlighting the error and suggesting the next possible action. The next loop is the image modification loop, where the user inputs are required. These inputs are desired classes for segmentation, the image resolution, and the representative slice number. Thereafter, the representative slice is displayed on a resizable pan-window inside the visualization panel shown in Figure 2. Further, an option to select a region of interest (ROI) is proposed, which can be accepted or rejected. If accepted, a REV is cropped from the 3D image stack based on user defined ROI dimensions. On rejection, the complete 3D stack is prepared for processing.

The next step is the segmentation process; an unsupervised or supervised algorithm is initialized based on the selection made by the user in the preprocessing *uitable*. Hereafter, the programming logic implemented at the data access layer (also know as back-end) for unsupervised and supervised segmentation schemes is briefly explained. It is an easy, one-step process in the case of unsupervised techniques i.e. based on the options selected in the preprocessing *uitable*, the image is filtered and subsequently, segmented. But, for unsupervised segmentation technique, Fuzzy C-means (FCM), an additional user input is required. A positive decimal number x, where x isequal to $1 \leq x \geq 2$ to set the membership criteria; when pixel values of different phases (ex. Rotligend sandstone, Gorsmont carbonate rock etc.) are in close vicinity or subsets of each other, FCM uses, the membership criteria to constain the segmentation 'loosely' or 'tightly' with the purpose to segregate different phases (Chauhan et al., 2016b).

In the case of supervised segmentation schemes (LSSVM, Bragging and Boosting) apriori information, also known as feature vector dataset or training dataset, is required to train the model(s) (Chauhan et al., 2016a; Chauhan et al., 2016b), and consequently, the trained model is ready to classify the rest of the dataset. The following five steps accomplish this procedure:

- First, the visualization panel displays a single 2D slice of the REV or 3D image stack in a resizable pan-window. The embedded *uimenu* in the pan-window offers to use the *subuimenu* opitons to feature vector selection, training and testing.
- Second, by pressing the *subuimenu* option *Pixel Selection*, the feature vector selection (FV) performs. The *Pixel Selection* callback function initializes the subroutine *uPixelSel()*, which sequentially displays a *uitable* in a resizeable pan-window. The *uitable* contains columns *Features*, *X-Coordinate*, and *Y-Coordinate*, which is for example the pixel coordinates of pore, matrix, minerals, noise/speaks. This is a mandatory step, to build the training dataset. The user enters this information in the respective columns of the *uitable*.
- In the third step, the user has to identify features, such as, pores, minerals, matrix, noise/specks, in the 2D image, using zoom in and out tools available in the toolbar. The X-coordinates and Y-coordinates of the identified features need to be extracted using the data cursor tool, also available in the toolbar. If satisfied, the user can enter, the features and the corresponding X,Y coordinates in the *Pixel Selection uitable*.
- In the fourth step, the data is gathered and exported for training. This is done by pressing the export button placed on the *uitable* pan-window; which initiates the subrountine *uExportTable( )*. The export subroutine collects a total of 36 (6 x 6) pixel values in the perimeter of the user specified X,Y coordinates in the *uitable*.
- In the fifth step, the model is trained. This is done by using the *subuimenu* in the 2D pan-window. As and when the *training* is finished, a notification appears on the *History* panel. Thereafter by pressing the *testing* option in the *subuimenu* the complete REV or 3D stack can be segmented.

A progress bar offers to monitor the state of process. Further, the *History* window displays information related to processing time, implemented image filters and the segmentation scheme. Finally, all relevant information and the segmented data is append to the main structure.

3.1.3. Visualisation Module

Once the processing is finished, the segmented data can be visualized in 2D format using *Plot* button or in 3D rendered stack using *VolRender* button. Figure 3 depicts the nested loop structure of the *Plot ( )* and *VolRender ( )* callback functions. On initialization, the *Plot( )* callback accesses the main structure, and plots the segmented 2D image of the segmented slice consecutive, in a resizable pan-window in the visualization panel. The displayed pan-window is embedded with a *uimenu* and corresponding *subuimenu*. The *uimenu* items and the *subuimenu* options are

- Geometrical Parameters → Porosity, Pore Size Distribution, Volume Fraction
- Performance → Entropy, Receiver Operational Characteristics (ROC), 10-fold Cross Validation
- Export Stack → ParaView, Raw

The methods used to calculate geometrical parameters and validation schemes are benchmarked in (Chauhan et al., 2016a) (Chauhan et al., 2016b). Therefore, the selection of desired options initialize respective subroutines (uPoreSzVol, uCalVal, uExport) and plot the results as shown in Figure 2. If required, the export of these parameters (Porosity, PSD, Volume Fraction, Entropy, ROC; 10-fold Cross Validation) is possible to Excel, ASCII or MATLAB® for further statistical analysis. Using the *Export Stack* item, the export of the 3D segmented volume to ParaView (.vtk files) or as .raw format files is feasible for the purpose of visualization or DRP analysis. The volume rendering functionalities of CobWeb 1.0 is simple in comparison to ParaView or DSI studio. The *VolRender ( )* function renders the 3D data set using orthogonal plane 2-D texture mapping technique (Heckbert, 1986) and is best suited for OpenGL hardware. The user has the option to render the 3D stack in the original resolution or at lower resolution; the lower resolution enhances the plotting speed but degrades the image quality by 10-folds. Due to this, we recommend to export the 3D stack to ParaView or DSI studio for visualization. This concludes the description of the section toolbox and functionalities. For more information on the usage of the graphical user interface the user manual can be consulted, which is available as supporting information.

In the following, sections the CobWeb toolbox is demonstrated by means of three showcase examples, which are briefly introduced in terms of underlying imaging settings, research question and challenges for image processing.

4. Materials and Methods

4.1. Gas-Hydrate bearing Sediment

The in-situ synchrotron-based tomography experiment and post-processing of synchrotron data conducted to resolve the microstructure of gas hydrate-bearing (GH) sediments is given in detail by Chaouachi et al. (2015), Falenty et al. (2015), and Sell et al. (2016). In brief, the tomographic scans were acquired with a monochromatic X-ray beam energy of 21.9 KeV at

Swiss Light Source (SLS) synchrotron facility (Paul-Scherrer-Institute, Villigen, Switzerland) using the TOMCAT beamline (Tomographic Microscope and Coherent Radiology Experiment; Stampanoni et al. 2006). Each tomogram was reconstructed from sinograms by using the gridded Fourier transformation algorithm (Marone und Stampanoni 2012). Later, a 3D stack of 2560 x 2560 x 2160 voxels (volume pixels) was generated resulting in a voxel resolution of 0.74 µm and 0.38 µm at 10-fold and 20-fold optical magnification.

4.1.1. Dual Filtering of Gas-Hydrate bearing Sediment

The ED artefact, is the high and low image contrast seen, between the edges, of the void, quartz and GH phases, in the GH tomograms. It certainly, aids in clear visual distinction, of these phases, but, becomes a nuisance during segmentation process. Several approaches to reduce ED artefact in GH tomograms and its effect on segmentation and numerical simulation have been discussed in (Sell et al., 2016). Based on our experience, a combination of the non-local means (NLM) filter and the anisotropic diffusion filter (AD), implemented using Avizo (ThermoFisher Scientific), works best in removing ED artefacts for our GH data. In short, AD was used for edge preservation and NLM for denoising. In this study, the NLM filter was set to a search window of 21, local neighbourhood of 6 and a similarity value of 0.71. The NLM filter was implemented in 3D mode to attain desired spatial and temporal accuracy and was processed on an CPU device.

4.1.2. Gas Hydrate (GH) bearing Sediment Dual Clustering

The edge enhancement ~~(ED)~~ effect was significant in all the reconstructed slices of the GH dataset. The ED effect was noticeable around the quartz grains, with high and low pixel intensities adjacent to each other. The high intensity pixel values (EDH) were very close to GH pixel values, while the low intensity pixel values (EDL) showed a variance between noise and void phase pixel values. Therefore, immediate segmentation performed on the pre-filtered GH datasets using CobWeb 1.0 resulted in misclassification. Further parameterizing and tuning the unsupervised (K-means) and supervised (LSSVM) modules of CobWeb 1.0 specifically, distance function (i.e., functions euclidean distance *sqeuclidean*, sum of absolute differences *cityblock*, and *mandist*) and different permutation and combination between of kernel type, bandwidth and cross-validation parameters, showed significant improvement, but the segmentation was still not optimal. The aim was to eliminate the ED features completely without altering the phase distribution between GH and the void. This prompted to develop a GH-specific workflow as explained below. The appendix provides the MATLAB® script for this workflow comprised of 6 steps:

Step 1: Filtering and REV selection

Four REVs of size 4 × 700^3 were cropped from the raw (16 bit) data stack. These REVs were dual-filtered using AD and NLM filters (see section 4.1.1). Figure 5 depicts a 2D dual-filtered image from REV1. In this study, the NLM filter was set to a search window of 21, local neighbourhood of 6 and a similarity value of 0.71. The NLM filter was implemented in 3D mode to attain desired spatial and temporal accuracy and was processed on an CPU device.

Step 2: K-means clustering

After, dual-filtration (Step 1), it was essential to segregate the noise, edge enhancement effects and different phases into labels of various classes. This was accomplished by K-means segmentation. In order to capture all the phases accurately along with noise and ED effects a segmentation process with up to twenty class labels was needed and performed. As a result class seven captured all the desired phases (noise, edge enhancement low intensities (EDL), void, quartz, edge enhancement high intensities (EDH), GH).

Step 3: Indexing

In the next step the purpose was to retrieve pixel values of various phases from the dual-filtered REV stacks. The indexing scheme is the following:

- First, through visual inspection of the segmented image (step 2) different phases and their corresponding labels where identified, shown in Table 1.
- Thereafter, pixel indices of these phases, where extracted from the segmented image based on their labels.
- Further, these indices where used as a reference mask to retrieve pixel values of the phases from the 16-bit raw REV stacks.

The obtained pixel values represent noise, void (liquid), EDL, quartz, EDH, and GH phases in the raw images. Then, histogram distribution of the pixel values in each phase was plotted. The skewness of the histograms was investigated where the max, min, mean and standard deviation for each of the histogram was calculated. Thereafter, max and min of the histograms where compared, and the indexing limits were adjusted, for as-long-as there was no overlap found amidst the histogram boundaries.

Step 4: Rescaling raw REV

~~Now,~~ In this step, the raw pixel values of the respective phases, i.e void, quartz, and GH, were replaced by their mean values, with an exception for EDH pixel values. The latter (EDH pixels) were replaced with the mean value of quartz. These assignments lead to optimal segregation of the phase boundaries in the raw dataset and finally to the elimination of the ED effect.

Step 5: K-means clustering

Finally, the re-scaled raw REV was segmented into three class labels using K-means segmentation to obtain the final result.

4.2. Grosmont Carbonate Rock

The digital rock images of the Grosmont carbonate rock were obtained from the FTP server GitHub (http://github.com/cageo/Krzikalla-2012) used in the benchmark study published by (Andrä et al., 2013a, 2013b). The

Grosmont carbonate rock was acquired from Grosmont formation Alberta, Canada. The Grosmont formation was deposited during upper Devonian and is divided into four facies members, LG UG-1, UG-2, and UG-3 (bottom to top). The sample was taken from UG-2 facies and is mostly composed of dolomite and karst breccia (Machel and Hunter, 1994; Buschkuehle et al., 2007). Laboratory measurements of porosity and permeability reported by (Andrä et al., 2013b) are around 21 % ($\phi = 0.21$) and $\kappa = 150$ mD − 470 mD, respectively. The Grosmont carbonate dataset was measured at the high-resolution X-ray computer tomographic facility of the University of Texas with an Xradia MicroXCT-400 instrument (ZEISS, Jena, Germany). The measurement was performed using 4x objective lenses, 70 kV polychromatic X-ray beam energy, and a 25 mm CCD detector. The tomographic images were reconstructed from the sinograms using proprietary software and corrected for the beam hardening effect, which is typical for lab-based polychromatic cone-beam X-ray instruments (Jovanović et al., 2013). The retrieved image volume was cropped to a dimension of 1024^3 with voxel size of 2.02 µm.

4.3. Berea Sandstone Rock

The Berea sandstone digital rock images were part of a benchmark project published by Andrä et al. (2013a, 2013b) and obtained from the *GitHub* FTP server. The Berea sandstone sample plug was acquired from Berea Sandstone Petroleum Cores ™ (Ohio USA). The porosity value of 20 % ($\phi = 0.20$) was obtained using a Helium pycnometer AccuPyc™ 1330 (Micromeritics Instrument Corp., Germany) and a Pascal-Mercury porosimeter (Thermo Scientific ™) as described in Giesche (2006). The permeability ranges between $\kappa = 200$ mD and $\kappa = 500$ mD as reported by Andrä et al. (2013b). Machel und Hunter (1994) identified minerals using a polarized optical microscope and a scanning electron microscope, and reported a mineral composition of Ankerite, Zircon, K-feldspar, Quartz, and Clay in the Berea sandstone sample. The synchrotron tomographic scans of Berea sandstone were also obtained at the SLS TOMCAT beamline. The beam energy was monochromatized to 26 keV for an optimal contrast with an exposure time of 500 ms. This resulted in a 3D tomographic stack with a dimension of 1024^3 voxels with a voxel size of 0.74 µm.

5. Result and Discussions

5.1. Data Selection

The represented elementary volume (REV) selection basically, was a combination of visual inspection and consecutively segmenting and plotting tends in relative porosity, pore size distribution and volume fraction. This was done by loading the complete stack in the CobWeb software, during the loading process a 2D movie of the tomogram is displayed in the display window and saved in the root folder. Carefully monitoring the movie gives an objective evaluation of the heterogeneity of the respective XCT sample. We observed, several sub-sample volumes at various location (X, Y) and depth (Z) inside the XCT tomograms. Thereafter, based on a subjective visual consensus different ROIs where selected, cropped, segmented and their respective geometrical parameter where intercompared. The main indicator, however, was the porosity trend; i.e when regression coefficient R2 value was close to zero, it was an indicator that its sub-volume has accumulated the heterogeneity along the z-axis of the sample. Therefore, based on the trend analysis approach, the sub-volume dimension were R2 value was close to zero was chosen as the suitable REV.

In the case of Berea sandstone, four different ROIs were investigated; whereas Grosmout carbonate rock seven different ROIs where need to identify the best REVs. Cubical stack size in between 300^3 to 700^3 slices were tested and later established that stack size around 480^3 suited the best. Through our previous scientific studies on the GH sediments (Sell et al., 2016; Sell et al., 2018) we were aware of the best-suited REVs and established that stack size of 700^3 was an appropriate stack size. The identification of best REV for Grosmout was relatively tedious compared to Berea sandstone and GH sediment; due to the low resolution and microporosity present in the Grosmount tomograms. Figure 4 shows the chosen ROIs of Berea, Grossmont and GH dataset and Figure 6 and Figure 8 show the surface plot for respective REVs.

5.2. Data Processing

In the case of Berea sandstone, the 3D reconstructed raw images (1024^3) had sufficient high resolution and contrast, thus did not show any noticeable change to the filtration. Whereas, the XCT images (1024^3) of the Grosmont carbonate rock needed a non-local means filtering which yielded in better visualization and performance results compared to those enhanced with anisotropic diffusion filter. However, for GH synchrotron dataset, the CobWeb 1.0 filters were insufficient to normalize the edge enhancement artifact ~~(ED)~~, several attempts were made to remove the edge enhancement effect using single filters and in combination with supervised techniques. But they did not yield desirable results. The edge enhancement artifact pixels values where in very close vicinity to the GH sediment pixels. Therefore, preprocessing with single filters despite using appropriate settings could not normalize enhancement artifact to a reasonable range of. Despite tailoring customized training dataset using a representative slice~~—~~ due to large standard deviation in the edge enhancement artifact values, GH was systematically misclassified as ED as the pixel values deviated away from trained model. Alternative approach was to create different training dataset using several representative slices, and introduce the unknow stack of data for classification in batches of 100 slices. This regularization trick for us did not represent a good norm for supervised ML classification.

Hence, through the experience gained in (Sell et al., 2016) for us dual-filtration was one of the best approaches we could include in preprocessing step. This dual-filtering did not removed the ED completely rather normalize it to a reasonable range. Through the approach of rescaling and (hard) K-means segmentation (dual-segmentation) we were absolutely sure that the ED artifact have been removed. ~~However for GH synchrotron dataset, the CobWeb 1.0 filters were insufficient to normalize the edge enhancement artifact (ED), therefore a unique~~ This dual filtering scheme ~~was implemented,~~ is explained in section 4.1.2. It is to be noted that, the NLM filter is hard-coded as 2D in the CobWeb standalone version (GUI). But, by tweaking or modifying the source code we could initially pre-processed the XCT images using NLM 3D filtration and thereafter subjected it to segmentation.

In general, our observation is that, depending on the resolution of the dataset, the fixed parameters of NLM and other filters should do a fairly good job. In case, their still exists noise and artefacts we recommended that the supervised techniques be used. The supervised techniques offer the possibility to select the residual noise or artefact pixel values before or after the filtration (pre-processing) through proper feature vector selection, and further training the appropriate model and performing classification. Through which, the existing noise and artefact can be isolated and segmented as separate labels. Another alternative option could be to pre-process the data with desired filters data and imported the data into CobWeb for segmentation and analysis.

Another issue ~~which needs to be discussed is the implementation of image segmentation~~ has to be explained in more detail is the implementation of the image segmentation. CobWeb 1.0 uses a slice-by-slice 2D approach. It was observed that the ML techniques tend to underestimate porosity values compared to manually segmented analysis at an REV scale size > 500^3. This substantial degree of uncertainty is caused due to 2D slice-by-slice processing rather than the ML techniques. The 2D slice-by-slice approach, passes only, the spatial information (X and Y coordinate direction) to the ML algorithms, and the ML algorithm ends up sorting the intensity variation in the spatial domain (local optimum). Therefore, the lack of ~~temporal~~ spatial information (Z coordinate direction) restricts the degree of freedom to find, a global ~~spatial-temporal~~ optimum. In other words, ~~as the temporal~~ changes ~~arise~~, due to bedding (sedimentary rock) or micro porosity (carbonate rocks) in the rock texture, ~~they~~ are represented as sudden spike or dip in porosity values; which appear as artefact or anomalies− and are often ~~more often then not~~ discarded. We acknowledge this issue and correction will be implemented in the future software version ~~in the next software version~~; in the current workflow it has not been accounted for (CobWeb 1.0). The 2D slice-by-slice processing scheme is much faster compared to the 3D approach. So, the choice of 2D processing for this research study was made to make it affordable to compute on desktop, laptop for near real-time and onsite evaluation. ~~And, the~~ The inaccuracies in porosities ~~is~~ are compensated by calculation of the mean porosity of the complete stack.

5.3. Multiphase Image Segmentation

The major problem for all multiphase segmentations is that phase having intermediate greyscale values gets sandwiched between two different phases. These intermediate phases sometimes represent some of the vital material property such as connectivity. Therefore, it is vital to emphasis, how ML can assist in issues related to multiphase segmentation. In a practical sense, machine learning tries to separate grayscale values in to disjoint sets. The creation of these disjoint sets is commonly done in two ways

1) By binning the greyscale values to the nearest representative values which is iteratively updated using an optimization function. This optimization function can be a simple regression or distance function (Jain et al., 1999), commonly used in the unsupervised techniques.

2) Second, by regularizing pre-trained models which store certain pattern information of the datasets such as topology features, contour intensities, pixel value etc. (Hopfield, 1982; Haykin, 1995; Suykens and Vandewalle, 1999). Or by using a voting system in a bootstrap ensemble of linear models (Breiman, 1996).

So, in this processes, the intermediate greyscale values which commonly have ~~low sample size~~ low volume fraction and exhibit Poisson distribution are merged in to larger sets of a high sample size to create disjoint boundaries. Through which the intermediate phase information misclassified and destroyed. One way to overcome this problem is by using, supervised techniques such as LSSVM or Ensemble classifiers. When constructing a training dataset (feature vector selection), careful selection of intermediate phases as a sufficiently large sample size compared to the predominate phases will preserve the intermediate phases. And, the likelihood that the trained model will identify them and cluster them separately is higher (Chauhan et al., 2016a). In this study, in particular, we made tests using supervised techniques (LSSVM, Ensemble classifies) and unsupervised technique (FCM) but the results weren't superior compared to K-means. Therefore, we choose K-means as it was faster compared to other ML techniques. Since we have used K-means for segmentation, it is necessary that we justify performance of K-means in terms of accuracy and speed. In the current research work, since we have used unsupervised technique, it safe to say that, accuracy and speed is directly proportional to starting point (initial location) in the segmentation process. Meaning, the closer the starting point (initial location) is to the global minima— faster will the algorithm converge and even so better is the performance (accuracy & speed). But, in unsupervised technique by default the choice of the starting point is through random seed unless explicitly specified. So, in the case of the dual segmentation approach used for segmentation, the intuition was to capture all the material phases, including the edge enhancement artefact, speck and noise etc. in the first step and thereafter in the second step to rescale them to the plausible phases. Hence, in the first step the 20 clusters where initialized using random seed. And, after the rescaling processes, we were aware of the initial locations which we used as starting point (initial location) to assist the algorithm to move towards identifying correct phases. Therefore, we could increase both the speed and accuracy of K-means.

5.4. Estimation of Relative Porosity and Pore Size Distribution

The pore size distribution (PSD) of the respective REVs were calculated using the CobWeb PSD module. The PSD module is based on an image processing morphological scheme (watershed transformation) suggested by Rabbani et al. (2014). As stated by Rabanni, in (Rabbani et al., 2014), the aim is to breakdown the monolithic void structure of rock into specific pores and throats connecting each other. (Rabbani et al., 2014) used unsegmented images and performed image filtration and thereafter segmented using watershed transformation. ~~In our case, the tomograms were already pre-processed and segmented using ML techniques and thereafter subjected to the watershed algorithm.~~ In our case, the tomograms were already pre-processed and segmented using ML techniques. These images are converted to binary images and thereafter subjected to the image processing distance function (Rosenfeld, 1969) and watershed algorithm (Myers et al., 2007) to extract pores and throats. City-block distance function is used to locate the void pixels (pores) and watershed with 8-connected neighborhood was used to obtain the interconnectivity. Since watershed algorithm is very sensitive to noise, despite the preprocessing and ML segmentation median filter was applied before subjecting to the watershed segmentation. Thereafter, the mean relative porosity value obtained for Berea sandstone is ϕ =17.3 ± 2.6 %, whereas for Grosmont carbonates the mean porosity value is lower (ϕ =10.5 ± 2.3 %) shown in Figure 6. Particularly, in the case of Grosmount, after segmentation the obtained porosity value ϕ =10.5 ± 2.3 % is extremely low compared to the laboratory measurement ϕ =21 % published in (Andrä et al., 2013a). Exact reason is not known, but could also be partly attributed to sub-resolution pores which couldn't be captured do to low resolution obtained through XCT measurement. The regression coefficient value of R^2 = 0.092 for the Berea sandstone porosity trend indicates that porosity remains constant throughout the REV sizes chosen, and therefore consolidated for scale-independent heterogeneities. In the case of Grosmont carbonate rock, the chosen REV size was the best out of five obtained, which consolidate again for scale-independent heterogeneities. The average pore size distribution thus obtained was 6.70 μm ± 0.68 μm and 14.21 μm ± 0.66 μm for Berea and Grosmont plug samples, respectively.

Similarly, the porosity and PSD of the four GH REVs were analyzed using CobWeb 1.0 and is shown in Figure 7. The low R^2 values of the porosity trends justify that, these GH REVs are scale-independent, and are an accurate representation of a large-scale system and are best suited for digital rock analysis. However, there is high variance compared with the mean PSD values. The exact reason is unknown, but may be due to the drastic increase and decrease of the quartz grains which can be seen in Figure 5. The first and last 2D slices of ROI 1 in Figure 5 show either non-isotropic or isotropic distribution of quartz grains, which might have contributed to the respective high and low standard deviation, seen in the porosity distribution. Figure 8 shows the surface and volume rendered plots of REV 1 and REV 2, due to the high accuracy of segmentation the quartz grain, brine and GH boundaries are clearly segregated and ED effect completely eliminated.

6. Conclusions and Outlook

This paper introduces with CobWeb 1.0 a new visualization and image analysis toolkit dedicated to representative elementary volume analysis of digital rocks. CobWeb 1.0 is developed on the MATLAB® framework and can be used as MATLAB® plugin or as a standalone executable. It offers robust image segmentation schemes based on machine learning (ML) techniques (unsupervised and supervised), were the accuracy of the segmentation schemes can be determined and results can be compared. Dedicated image processing filters such as the non-local means, anisotropic diffusion, averaging and the contrast enhancement functions help to reduce artefacts and increase the signal-to-noise ratio. The petrophysical and geometrical properties such as porosity, pore size distribution and volume fractions can be computed quickly on a single representative 2D slice or on a complete 3D stack. This had been validated using synchrotron datasets of the Berea sandstone (at a spatial resolution of 0.74 μm), a gas hydrate-bearing sediment (0.76 μm) and a high resolution lab-based cone-beam tomography dataset of the Grosmont Carbonate rock (2.02 μm). The gas hydrate dataset, despite its nanoscale resolution, was hampered with strong edge enhancement ~~(ED)~~ artefacts~~, which causes discrepancies in modelling and transport simulation~~. A combination of the dual filtering and dual clustering approach is proposed to completely eliminate the ED effect in the gas hydrate sediments, and the code is attached as an appendix. The REV studies performed on Berea sandstone, Grosmont carbonate rock and GH sediment using CobWeb1.0 shows relative porosity trends with very low linear regression values of 0.092, 0.1404, 0.0527 respectively. CobWeb1.0 ability to acurately segment data without compromise on the data quality at a resonable speed makes it an favorable tool for REV analysis.

CobWeb1.0 is still somewhat limited regarding its volume rendering capabilities, which will be one of the features to improve in the next version. The volume rendering algorithms implemented in CobWeb 1.0 so far do not reach the capabilities offered by ParaView or DSI studio, which relies on the OpenGL marching cube scheme. At present, the densely nested loop structure appears to be the best choice for systematic processing. As an outlook, vectorization and indexing approaches (*bsxfun*, *repmat*) have to be checked in detail to improve on processing speed. MATLAB® —Java synchronization will be explored further to configure issues related to multi-threading and visualization (Java OpenGL). Furthermore, a module CrackNet (crack network) is planned to be implemented, which will explicitly tackle the segmentation of cracks and fissures in geomaterials using machine learning techniques and a mesh generation plugin (stl format) for 3D printing. Pore network extraction and skeletonization schemes such as modified maximum ball algorithm (Arand and Hesser, 2017) and medial axis transformation (Katz and Pizer, 2003) will be considered such that the data can be exported to open-source pore network modelling packages such as Finite-difference method Stokes solver (FDMSS) for 3D pore geometries and OpenPNM (Gerke et al., 2018; Gostick, 2017; Gostick et al., 2016) . ~~(Gostick et al., 2016; Gostick, 2017; Gerke et al., 2018).~~

Code availability / Data availability

With regards to the code availability, the MATLAB® code for removal of edge enhancement artifacts from the gas hydrate bearing sediment is attached as appendix. The CobWeb executable as well as the user manual and The gas-hydrate bearing sediment, XCT datasets are available to public on Zenodo repository http://dx.doi.org/10.5281/zenodo.2390943.

The CobWeb executable requires a MATLAB® runtime compiler R2017b (9.3), which can be downloaded and installed from https://ch.mathworks.com/products/compiler/MATLAB®-runtime.html. The XCT dataset of Berea Sandstone and Grosmount Carbonate Rock can be obtained from *GitHub* FTP server (http://github.com/cageo/Krzikalla-2012). The gas-hydrate XCT datasets are not publicly available.

Author contribution

Contributor Roles Taxonomy (CrediT) is used to specify author contribution. https://casrai.org/credit/.

Swarup Chauhan conceptualized, investigated and performed the study. Further, implemented the machine learning workflow and graphical user interface design. Additionally, Swarup Chauhan performed the formal analysis and developed a software code for the removal of the edge enhancement artefact using the dual clustering approach. Further contributions of Swarup Chauhan: data curation on of the CobWeb software, writing the software manual, figures and writing, reviewing and editing the manuscript.

Kathleen Sell conceptualized, investigated and performed a case study on gas hydrates. Further, performed a study on the removal of edge enhancement artefacts and phase segmentation of methane hydrate X-ray tomograms (XCT). Also, she did a formal analysis by implementing dual filtration approach to reduce the edge enhancement artefacts. Kathleen Sell participated in discussions to validate phase segmentation using the dual segmentation approach and was involved in writing, reviewing and editing the manuscript

~~Frieder Enzmann was involved in the investigation of the X-ray tomography experiments and in acquiring synchrotron radiation beam time (TOMCAT beamline) at Paul Scherrer Institute, Villigen, Switzerland. He performed the reconstruction of XCT tomograms. Provided data curation in the form of archiving and maintenance - initial and later re-use for the XCT data.~~

Wolfram Rühaak was involved in the project administration of the CobWeb activities, provided resources with respect to graphical user interface (GUI) and inputs on improving GUI functionalities.

Thorsten Wille was involved in funding acquisition and sponsoring the CobWeb project, under the framework of the SUGAR (Submarine Gashydrat Ressourcen) III project by the Germany Federal Ministry of Education and Research grant number: 03SX38IH. He was involved in project administration and provided feedback on GUI functionalities

Ingo Sass was involved in the concept and funding acquisition for the CobWeb project, under the framework of the SUGAR (Submarine Gashydrat Ressourcen) III project by the Germany Federal Ministry of Education and Research (grant number: 03SX38IH). He also provided supervision, project administration, resources and periodic review to improve GUI functionalities.

~~Michael Kersten was involved in conceptualization, preliminary investigation, funding acquisition for the project "Poroelastic wave propagation modelling on gas hydrate-bearing sediment based on tomographic microstructure data" from Deutsche Forschungsgemeinschaft (DFG grant number Ke 508/20 and Ku 920/18). He provided supervision, resources and was involved in writing, review and editing of the manuscript.~~

Acknowledgements

We thank Heiko Andrä and his team at Fraunhofer ITWM, Kaiserslautern, Germany, for providing us with the synchrotron tomography benchmark dataset of the Berea sandstone. We also thank Michael Kersten, Frieder Enzmann and his group at the Institute for Geoscience, Johannes-Gutenberg Universität Mainz, for providing high resolution gas hydrate sxnchroton-data. The acquisition of the gas hydrate synchrotron-data was funded by the German Science Foundation (DFG grant Ke 508/20 and Ku 920/18). This study was funded within the framework of the SUGAR (Submarine Gashydrat Ressourcen) III project by the Germany Federal Ministry of Education and Research (BMBF grant 03SX38IH). The sole responsibility of the paper lies with the authors.

7. References

A. Buades, B. Coll, and J. M. Morel: A non-local algorithm for image denoising, in: 2005 IEEE Computer Society Conference on Computer Vision and Pattern Recognition (CVPR'05), 60-65 vol. 2, 2005.

Al-Raoush, R. and Papadopoulos, A.: Representative elementary volume analysis of porous media using X-ray computed tomography, Powder Technology, 200, 69–77, doi:10.1016/j.powtec.2010.02.011, 2010.

Altman, Y.: Accelerating MATLAB Performance, CRC Press, 2014.

Andrä, H., Combaret, N., Dvorkin, J., Glatt, E., Han, J., Kabel, M., Keehm, Y., Krzikalla, F., Lee, M., Madonna, C., Marsh, M., Mukerji, T., Saenger, E. H., Sain, R., Saxena, N., Ricker, S., Wiegmann, A., and Zhan, X.: Digital rock physics benchmarks—Part I: Imaging and segmentation, Benchmark problems, datasets and methodologies for the computational geosciences, 50, 25–32, doi:10.1016/j.cageo.2012.09.005, 2013a.

Andrä, H., Combaret, N., Dvorkin, J., Glatt, E., Han, J., Kabel, M., Keehm, Y., Krzikalla, F., Lee, M., Madonna, C., Marsh, M., Mukerji, T., Saenger, E. H., Sain, R., Saxena, N., Ricker, S., Wiegmann, A., and Zhan, X.: Digital rock physics benchmarks—part II: Computing effective properties, Benchmark problems, datasets and methodologies for the computational geosciences, 50, 33–43, doi:10.1016/j.cageo.2012.09.008, 2013b.

Arand, F. and Hesser, J.: Accurate and efficient maximal ball algorithm for pore network extraction, Comput. Geosci., 101, 28–37, doi:10.1016/j.cageo.2017.01.004, 2017.

Bezdek, J. C., Hathaway, R. J., Sabin, M. J., and Tucker, W. T.: CONVERGENCE THEORY FOR FUZZY C-MEANS: COUNTEREXAMPLES AND REPAIRS, IEEE Transactions on Systems, Man and Cybernetics, 17, 873–877, 1987.

Bishop, C. M.: Pattern Recognition and Machine Learning (Information Science and Statistics), Springer-Verlag, Berlin, Heidelberg, 2006.

Bradley, A. P.: The use of the area under the ROC curve in the evaluation of machine learning algorithms, Pattern Recognition, 30, 1145–1159, doi:10.1016/S0031-3203(96)00142-2, 1997.

Breiman, L.: Bagging predictors, Machine Learning, 24, 123–140, doi:10.1007/BF00058655, 1996.

Buschkuehle, B. E., Hein, F. J., and Grobe, M.: An Overview of the Geology of the Upper Devonian Grosmont Carbonate Bitumen Deposit, Northern Alberta, Canada, Natural Resources Research, 16, 3–15, doi:10.1007/s11053-007-9032-y, 2007.

Chauhan, S., Rühaak, W., Anbergen, H., Kabdenov, A., Freise, M., Wille, T., and Sass, I.: Phase segmentation of X-ray computer tomography rock images using machine learning techniques: an accuracy and performance study, Solid Earth, 7, 1125–1139, doi:10.5194/se-7-1125-2016, 2016a.

Chauhan, S., Rühaak, W., Khan, F., Enzmann, F., Mielke, P., Kersten, M., and Sass, I.: Processing of rock core microtomography images: Using seven different machine learning algorithms, Computers & Geosciences, 86, 120–128, doi:10.1016/j.cageo.2015.10.013, 2016b.

Cnudde, V. and Boone, M. N.: High-resolution X-ray computed tomography in geosciences: A review of the current technology and applications, Earth-Science Reviews, 123, 1–17, doi:10.1016/j.earscirev.2013.04.003, 2013.

Costanza-Robinson, M. S., Estabrook, B. D., and Fouhey, D. F.: Representative elementary volume estimation for porosity, moisture saturation, and air-water interfacial areas in unsaturated porous media: Data quality implications, Water Resour. Res., 47, doi:10.1029/2010WR009655, 2011.

Dietterich, T. G.: Approximate Statistical Tests for Comparing Supervised Classification Learning Algorithms, Neural Computation, 10, 1895–1923, doi:10.1162/089976698300017197, 1998.

Dunn, J. C.: A Fuzzy Relative of the ISODATA Process and Its Use in Detecting Compact Well-Separated Clusters, Journal of Cybernetics, 3, 32–57, doi:10.1080/01969727308546046, 1973.

Gerke, K. M., Vasilyev, R. V., Khirevich, S., Collins, D., Karsanina, M. V., Sizonenko, T. O., Korost, D. V., Lamontagne, S., and Mallants, D.: Finite-difference method Stokes solver (FDMSS) for 3D pore geometries: Software development, validation and case studies, Benchmark problems, datasets and methodologies for the computational geosciences, 114, 41–58, doi:10.1016/j.cageo.2018.01.005, 2018.

Gitman, I. M., Gitman, M. B., and Askes, H.: Quantification of stochastically stable representative volumes for random heterogeneous materials, Archive of Applied Mechanics, 75, 79–92, doi:10.1007/s00419-005-0411-8, 2006.

Gostick, J., Aghighi, M., Hinebaugh, J., Tranter, T., Hoeh, A, Michael, Day, H., Spellacy, B., Sharqawy, H, Mostafa, Bazylak, A., Burns Alan, Lehnert, W., and Putz, A.: OpenPNM: A Pore Network Modeling Package, Computing in Science & Engineering, 18, 60–74, doi:10.1109/MCSE.2016.49, 2016.

Gostick, J. T.: Versatile and efficient pore network extraction method using marker-based watershed segmentation, Phys. Rev. E, 96, 23307, doi:10.1103/PhysRevE.96.023307, 2017.

Haykin, S. S.: Neural networks: A comprehensive foundation, [Nachdr.], Macmillan, New York, NY, 696 pp., 1995.

Heckbert, P. S.: Survey of Texture Mapping, IEEE Computer Graphics and Applications, 6, 56–67, doi:10.1109/MCG.1986.276672, 1986.

Hopfield, J. J.: Neural networks and physical systems with emergent collective computational abilities, Proc Natl Acad Sci USA, 79, 2554, doi:10.1073/pnas.79.8.2554, 1982.

Iassonov, P., Gebrenegus, T., and Tuller, M.: Segmentation of X-ray computed tomography images of porous materials: A crucial step for characterization and quantitative analysis of pore structures, Water Resour. Res., 45, doi:10.1029/2009WR008087, 2009.

Jain, A. K.: Data clustering: 50 years beyond K-means, Pattern Recognition Letters, 31, 651–666, doi:10.1016/j.patrec.2009.09.011, 2010.

Jain, A. K., Murty, M. N., and Flynn, P. J.: Data Clustering: A Review, ACM Comput. Surv., 31, 264–323, doi:10.1145/331499.331504, 1999.

Jovanović, Z., Khan, F., Enzmann, F., and Kersten, M.: Simultaneous segmentation and beam-hardening correction in computed microtomography of rock cores, Computers and Geosciences, 56, 142–150, doi:10.1016/j.cageo.2013.03.015, 2013.

Kaestner, A., Lehmann, E., and Stampanoni, M.: Imaging and image processing in porous media research, Quantitative links between porous media structures and flow behavior across scales, 31, 1174–1187, doi:10.1016/j.advwatres.2008.01.022, 2008.

Katz, R. A. and Pizer, S. M.: Untangling the Blum Medial Axis Transform, International Journal of Computer Vision, 55, 139–153, doi:10.1023/A:1026183017197, 2003.

Leu, L., Berg, S., Enzmann, F., Armstrong, R. T., and Kersten, M.: Fast X-ray Micro-Tomography of Multiphase Flow in Berea Sandstone: A Sensitivity Study on Image Processing, Transport in Porous Media, 105, 451–469, doi:10.1007/s11242-014-0378-4, 2014.

Machel, H. G. and Hunter, I. G.: Facies models for middle to late devonian Shallow-Marine carbonates, with comparisons to modern reefs: a guide for facies analysis, Facies, 30, 155–176, doi:10.1007/BF02536895, 1994.

MacQueen, J. (Ed.): Some methods for classification and analysis of multivariate observations, Fifth Berkeley Symposium on Mathematical Statistics and Probability, University of California Press, 281-297, 1967.

Mjolsness, E. and DeCoste, D.: Machine Learning for Science: State of the Art and Future Prospects, Science, 293, 2051, doi:10.1126/science.293.5537.2051, 2001.

Myers, G. R., Mayo, S. C., Gureyev, T. E., Paganin, D. M., and Wilkins, S. W.: Polychromatic cone-beam phase-contrast tomography, Phys. Rev. A, 76, 45804, doi:10.1103/PhysRevA.76.045804, 2007.

P. Perona and J. Malik: Scale-space and edge detection using anisotropic diffusion, IEEE Transactions on Pattern Analysis and Machine Intelligence, 12, 629–639, doi:10.1109/34.56205, 1990.

Parker, J. R.: Algorithms for Image Processing and Computer Vision, Wiley, 2010.

Porter Mark L., Wildenschild Dorthe, Grant Gavin, and Gerhard Jason I.: Measurement and prediction of the relationship between capillary pressure, saturation, and interfacial area in a NAPL-water-glass bead system, Water Resour. Res., 46, doi:10.1029/2009WR007786, 2010.

Rabbani, A., Jamshidi, S., and Salehi, S.: An automated simple algorithm for realistic pore network extraction from micro-tomography images, Neural network applications to reservoirs: Physics-based models and data models, 123, 164–171, doi:10.1016/j.petrol.2014.08.020, 2014.

Razavi, M., Muhunthan, B., and Al Hattamleh, O.: Representative Elementary Volume Analysis of Sands Using X-Ray Computed Tomography, Geotechnical Testing Journal, 30, 212–219, doi:10.1520/GTJ100164, 2007.

Rosenfeld, A.: Picture Processing by Computer, ACM Comput. Surv., 1, 147–176, doi:10.1145/356551.356554, 1969.

Schlüter, S., Sheppard, A., Brown, K., and Wildenschild, D.: Image processing of multiphase images obtained via X-ray microtomography: A review, Water Resour. Res., 50, 3615–3639, doi:10.1002/2014WR015256, 2014.

Sell, K., Quintal, B., Kersten, M., and Saenger, E. H.: Squirt flow due to interfacial water films in hydrate bearing sediments, Solid Earth, 9, 699–711, doi:10.5194/se-9-699-2018, 2018.

Sell, K., Saenger, E. H., Falenty, A., Chaouachi, M., Haberthür, D., Enzmann, F., Kuhs, W. F., and Kersten, M.: On the path to the digital rock physics of gas hydrate-bearing sediments – processing of in situ synchrotron-tomography data, Solid Earth, 7, 1243–1258, doi:10.5194/se-7-1243-2016, 2016.

Shreyamsha Kumar, B. K.: Image denoising based on non-local means filter and its method noise thresholding, Signal, Image and Video Processing, 7, 1211–1227, doi:10.1007/s11760-012-0389-y, 2013.

Smith, S. M. and Brady, J. M.: SUSAN—A New Approach to Low Level Image Processing, International Journal of Computer Vision, 23, 45–78, doi:10.1023/A:1007963824710, 1997.

Suykens, J. A. K. and Vandewalle, J.: Least Squares Support Vector Machine Classifiers, Neural Processing Letters, 9, 293–300, doi:10.1023/A:1018628609742, 1999.

T. M. Cover: Geometrical and Statistical Properties of Systems of Linear Inequalities with Applications in Pattern Recognition, IEEE Transactions on Electronic Computers, EC-14, 326–334, doi:10.1109/PGEC.1965.264137, 1965.

van Gestel, T., Suykens, J. A. K., Baesens, B., Viaene, S., Vanthienen, J., Dedene, G., Moor, B. de, and Vandewalle, J.: Benchmarking Least Squares Support Vector Machine Classifiers, Mach. Learn., 54, 5–32, doi:10.1023/B:MACH.0000008082.80494.e0, 2004.

Zadeh, L. A.: Fuzzy sets, Information and Control, 8, 338–353, doi:10.1016/S0019-9958(65)90241-X, 1965.

Zhang D, Zhang R, Chen S, and Soll, W. E.: Pore scale study of flow in porous media: Scale dependency, REV, and statistical REV, Geophys. Res. Lett., 27, 1195–1198, doi:10.1029/1999GL011101, 2000.

Table 1: Class labels of different phases

Labels	**Phases**
0	Noise
1 and 3	Void (liquid)
2	Edge enhancement low intensities (EDL)
4	Quartz
5	Edge enhancement high intensities (EDL)
6 and 7	Gas hydrate

Figures

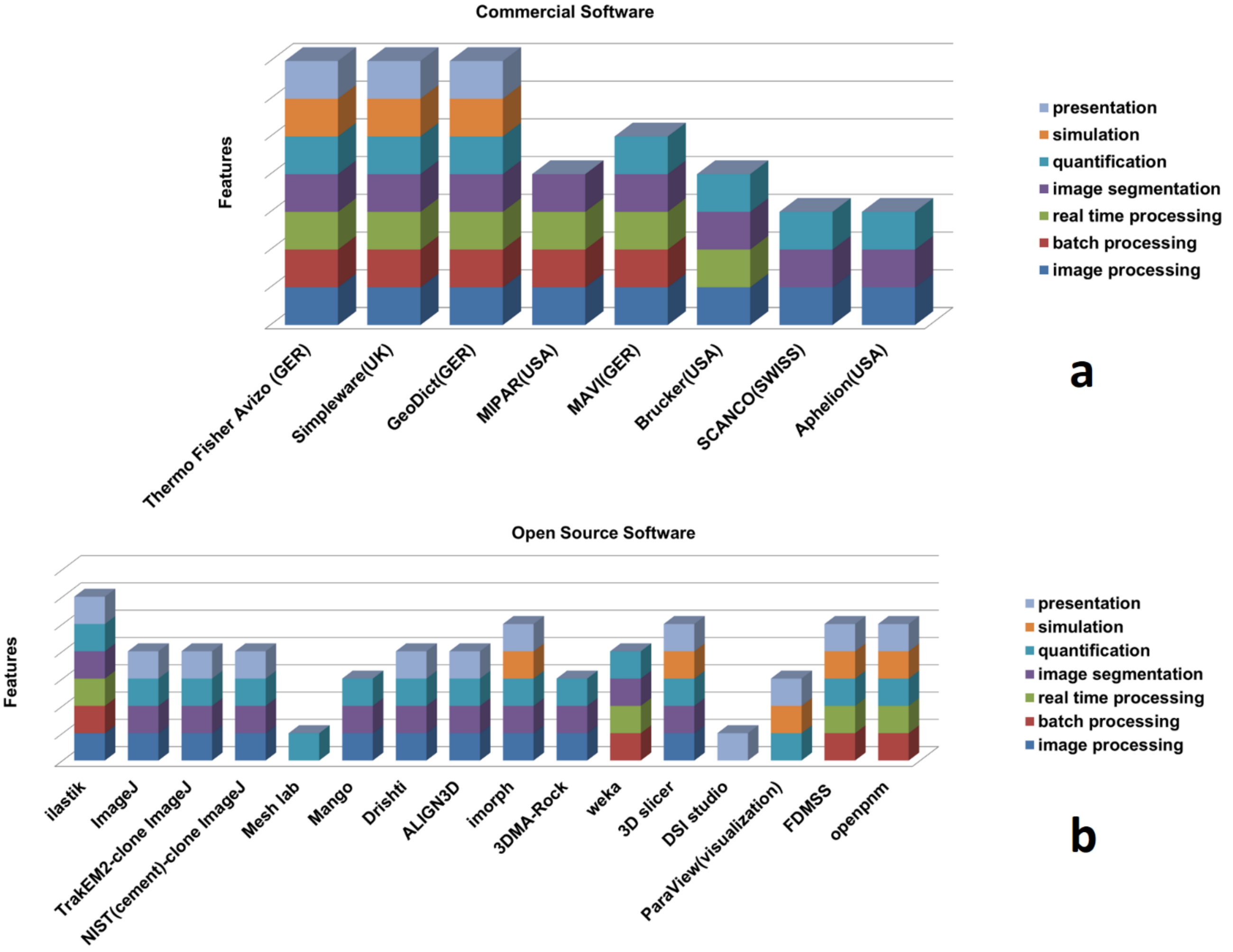

Figure 1: Market survey of the currently available commercial software (a) and open source software (b) assisting in digital rock physics analysis with features as indicated in legend

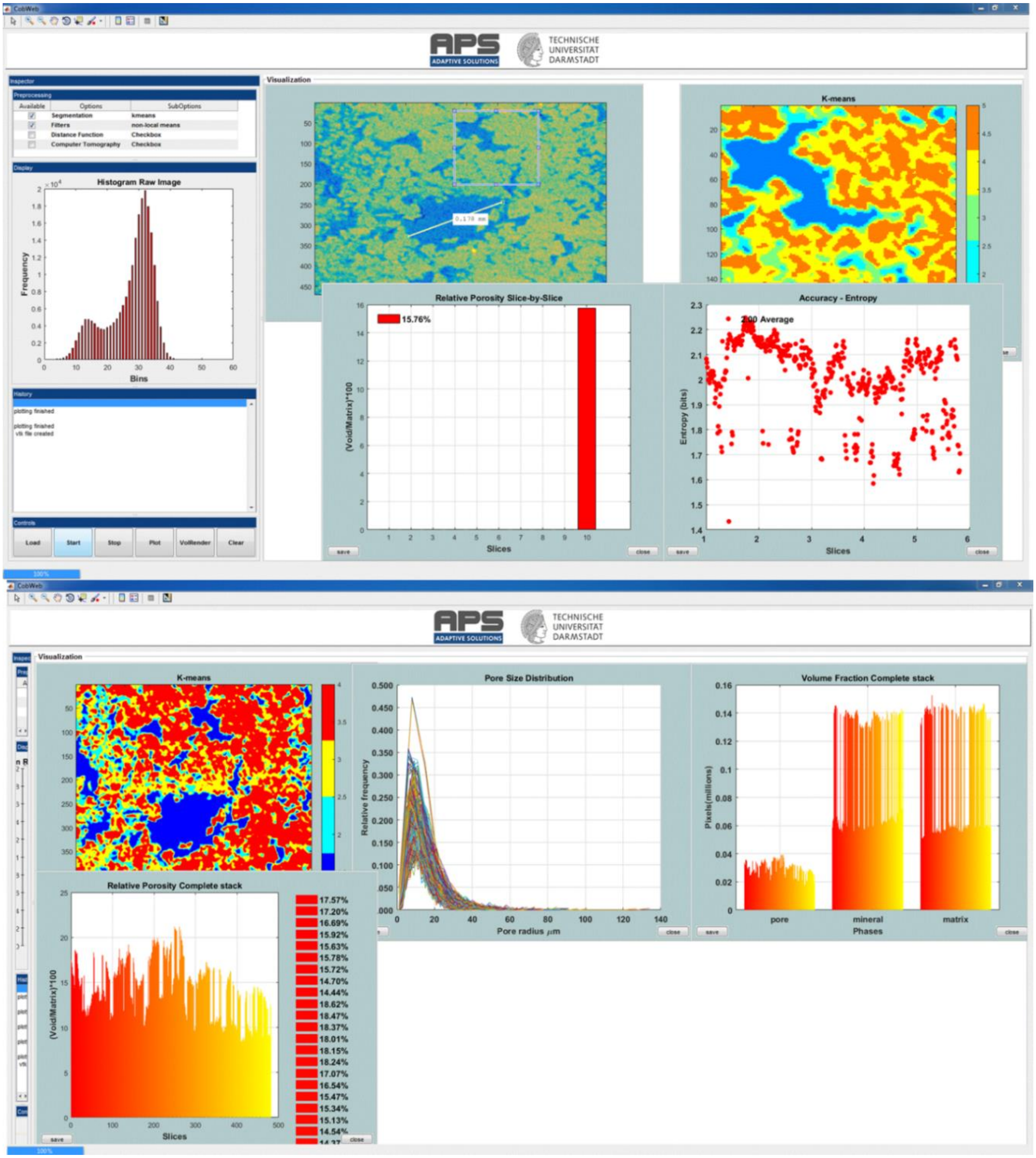

Inspector

Preprocessing

Available	Options	SubOptions
☑	Segmentation	kmeans
☑	Filters	non-local means
□	Distance Function	Checkbox
□	Computer Tomography	Checkbox

History

plotting finished

plotting finished
vtk file created

Figure 2: Snapshots of the CobWeb GUI. XCT stack of Grosmont Carbonate rock is shown as an example for representative elementary volume analysis. The top panel displays the XCT raw sample, the K-means segmented ROI, and the porosity of single slice No. 10. The bottom plot shows pore size distribution of the complete REV stack, the relative porosity and volume fraction, respectively

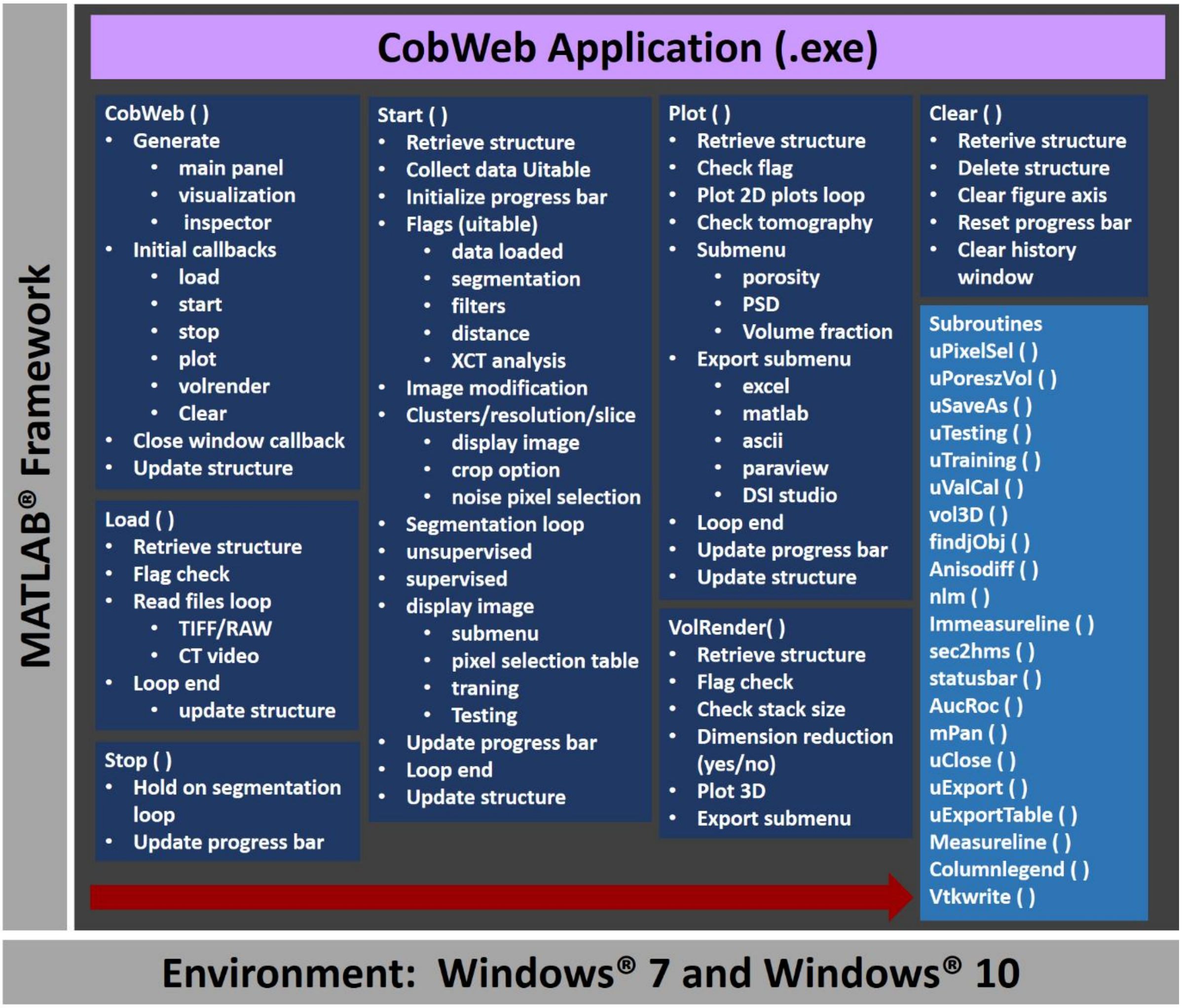

Figure 3: The general workflow of the CobWeb software tool, where the arrow denotes the series in which different modules (represented in dark blue boxes) are compiled and executed. A separate file script is used to generate .dll binaries and executables

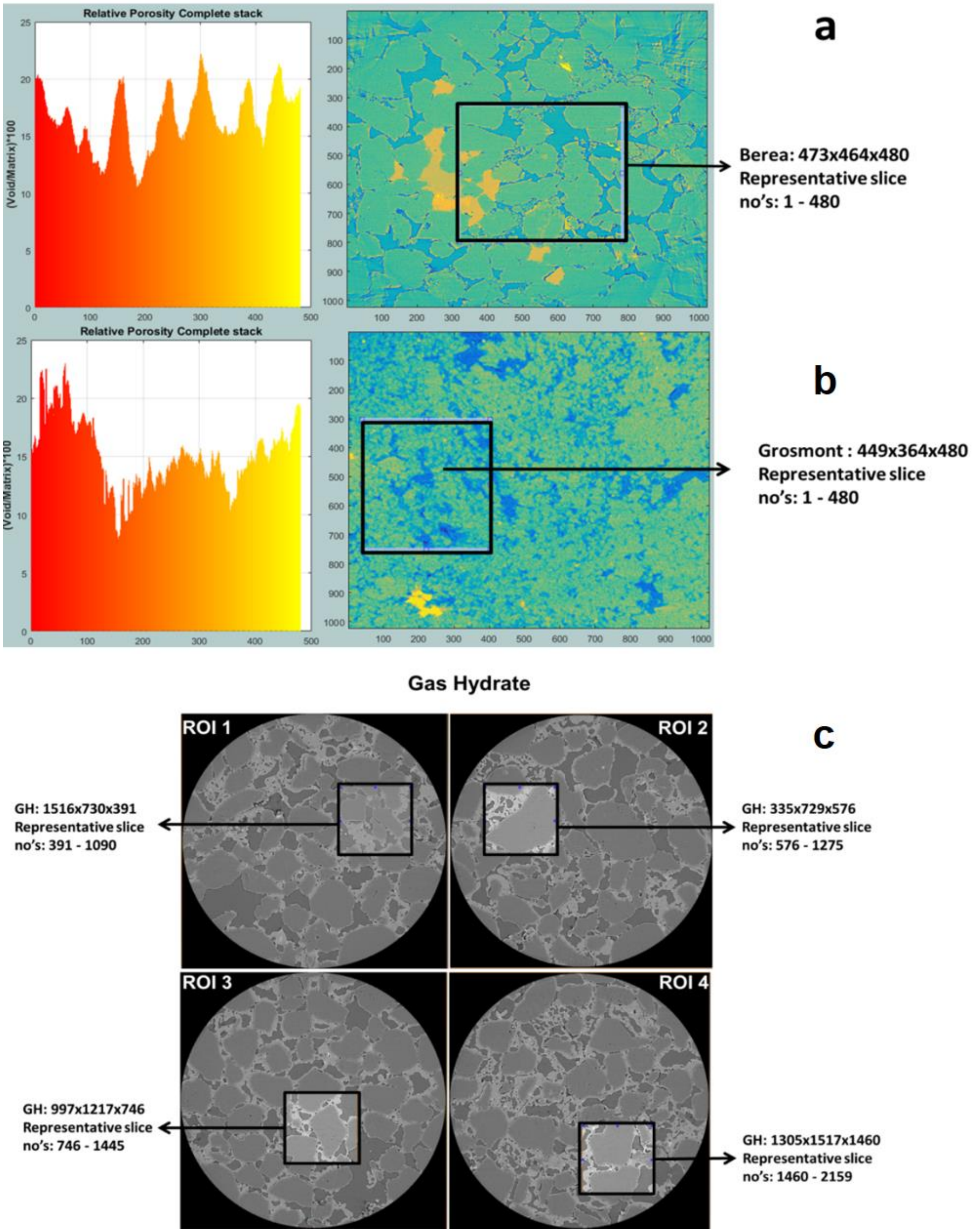

Figure 4: The most suitable ROIs and corresponding REV dimensions of Berea sandstone and Grosmont carbonate Gas Hydrate-bearing sediment is shown in the panel a b and c respectively

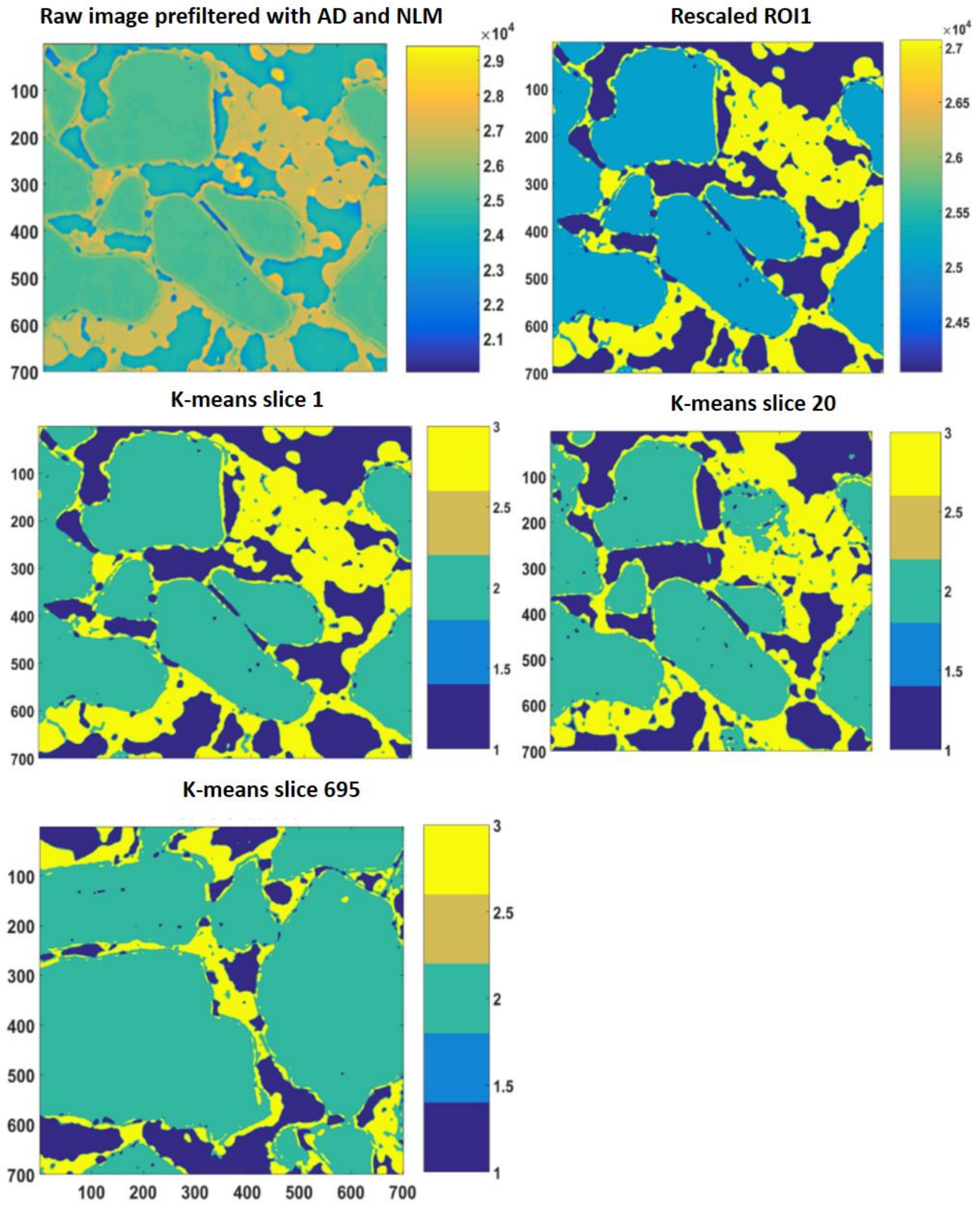

Raw image prefiltered with AD and NLM

Rescaled ROI1

K-means slice 1

K-means slice 20

K-means slice 695

Figure 5: 2D slices of REV 1 are represented above. The raw image is first filtered with anisotropic diffusion filtered and later on with non-local means. Thereafter, the different phases where segregated using a segmentation and indexing approach and the raw image(s) is rescaled such that they aren't any overlap or mixed phases within the raw image; and example is shown as the rescaled

2D ROI plot. Thereafter K-means segmentation is performed on the complete stack; 2D images of slice 1, slice 20 and slice 695 are shown as examples.

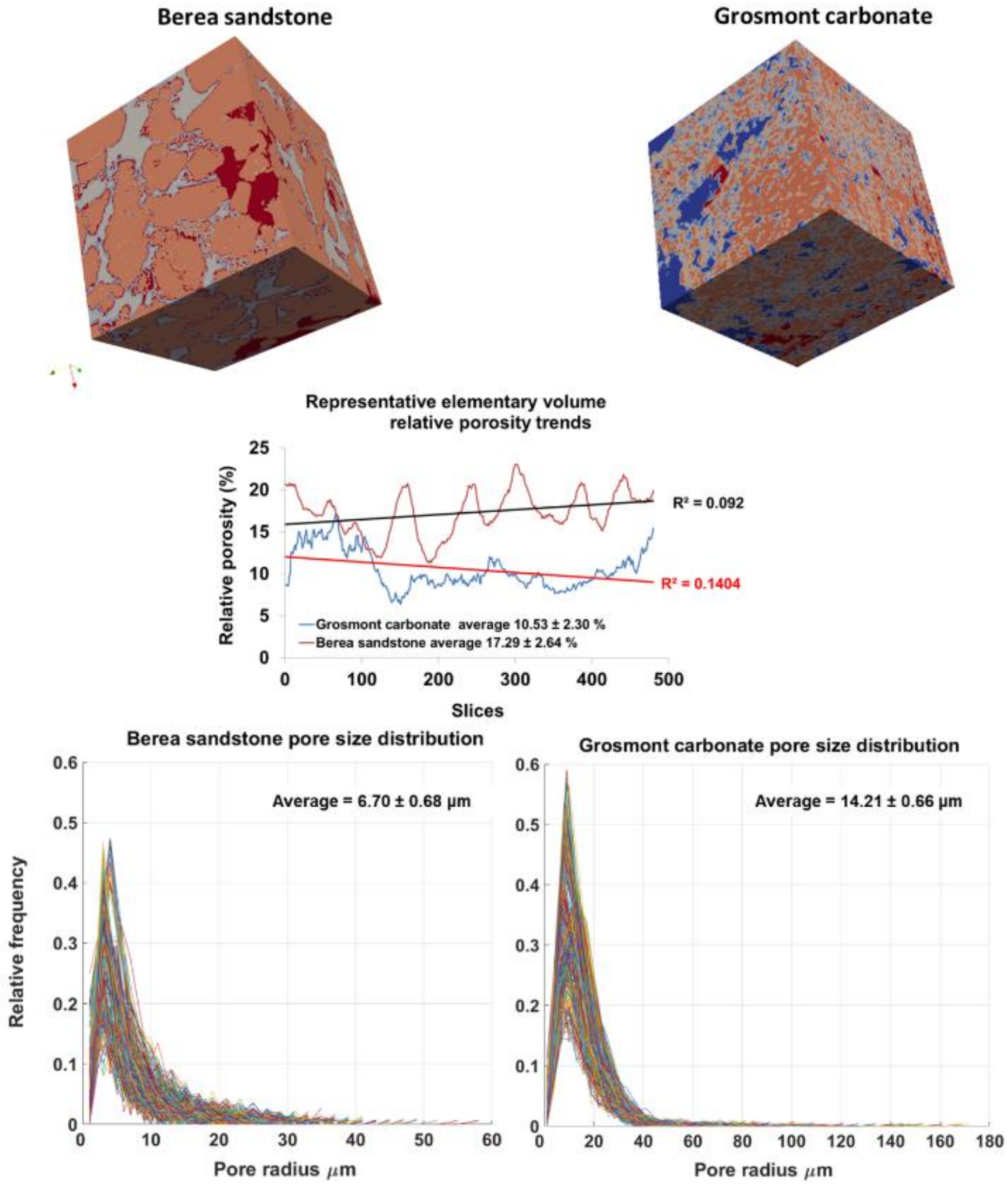

Figure 6: Top panel shows surface plot of REVs Berea sandstone and Grosmont carbonate (size 471x478x480) using visualisation software ParaView. Middle plot shows the relative porosity (%) trend for Berea sandstone and Grosmont carbonate REVs samples. Bottom plot shows the pore size distribution of Berea sandstone and Grosmont carbonate. XCT images were segmented using K-means. In the case of Grosmont, a non-local means filter was used

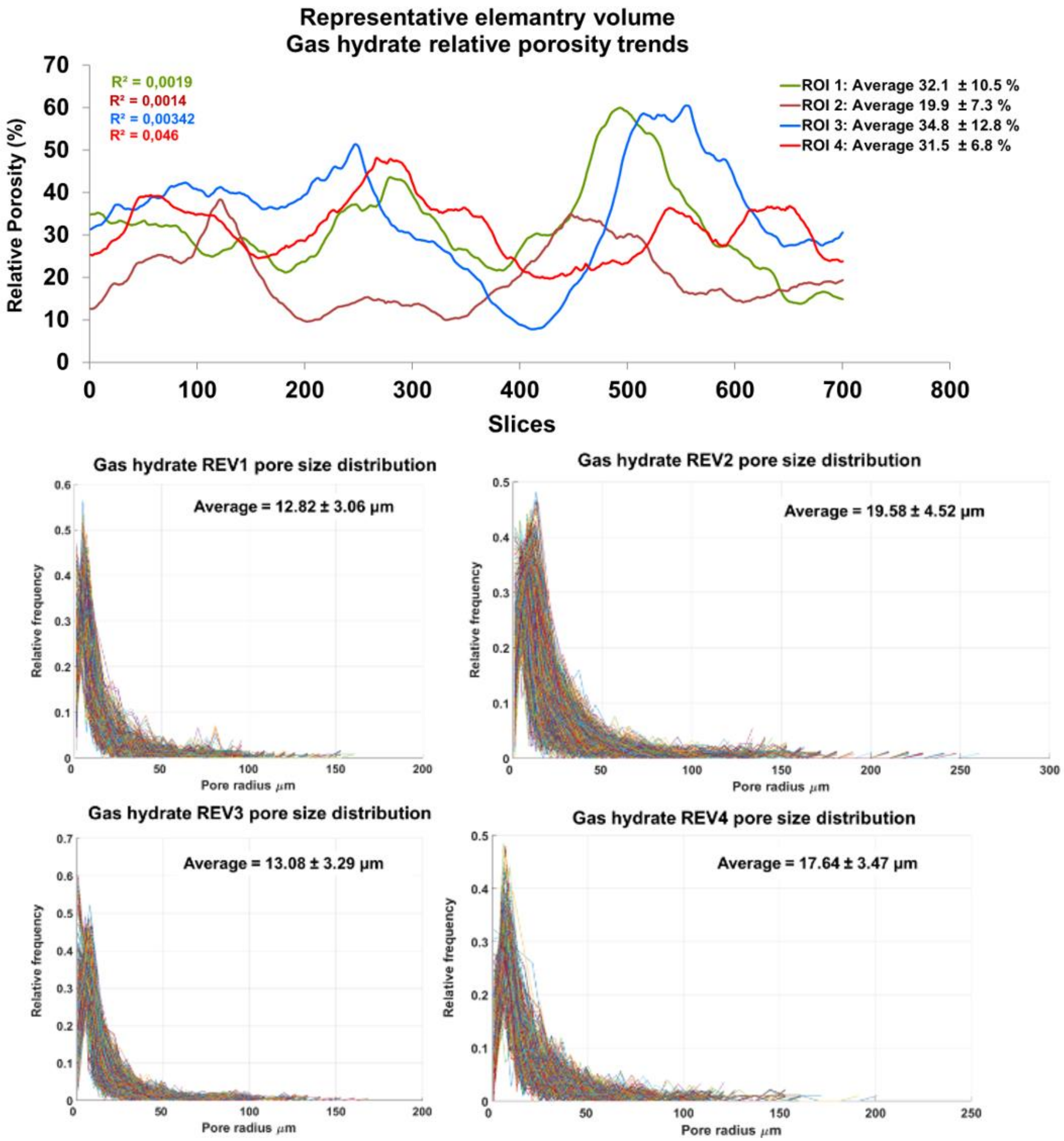

Figure 7: The top panel shows relative porosity trend analysis of gas hydrates, the middle and bottom panel show the geometrical pore size distribution of the respective REVs. The analysis was performed using CobWeb 1.0

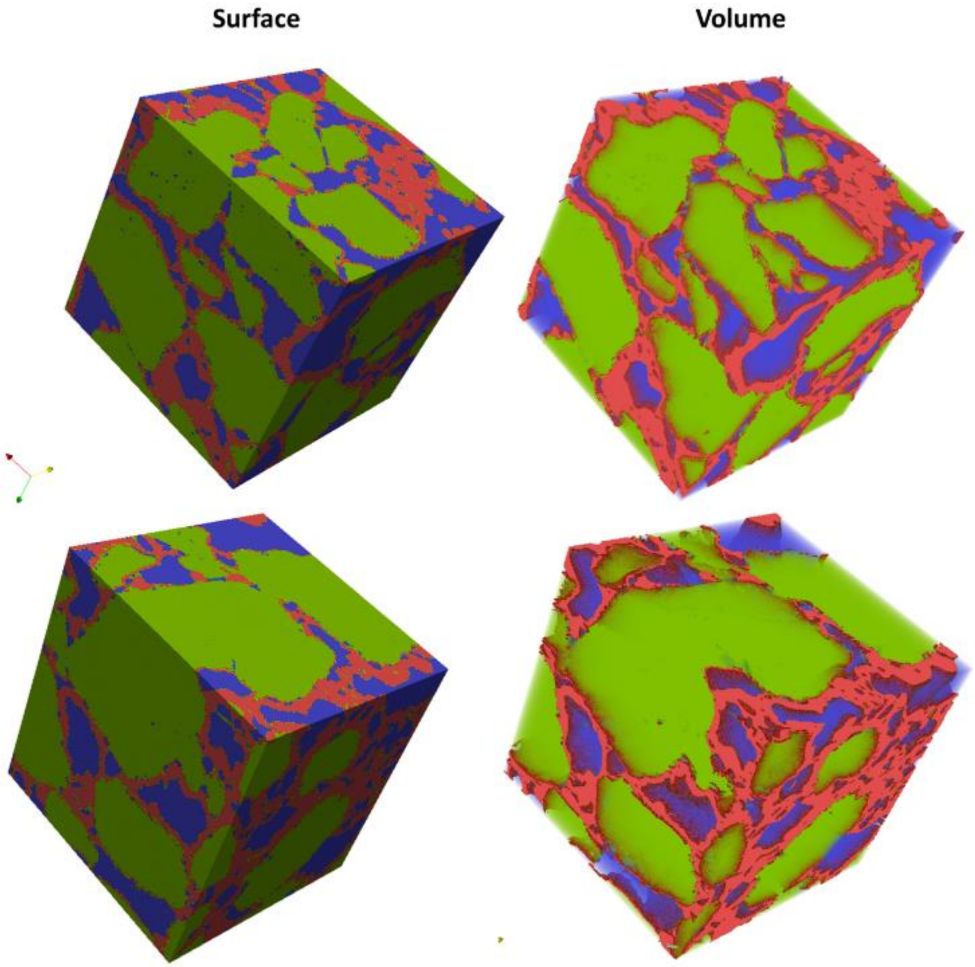

Figure 8: Segmented REVs of a gas hydrate sample displayed as surface and volume rendered. Analyzed using CobWeb 1.0 and exported to VTK format using CobWeb 1.0 ParaView plug-in. Quartz grain phase is represented in green color, gas hydrate in red, and in blue is the void space.